Final Technical Report (FTR) Instructions

Solar Energy Technologies Office

Final Report Template

Project Title:	Volumetrically Absorbing Thermal Insulator (VATI) for High-temperature Receivers
Project Period:	02/01/19 – 1/31/21
Project Budget:	$500,000
Submission Date:	3/17/21
Recipient:	The University of Utah
Address:	201 S Presidents Circle
	Salt Lake City, UT 84112-9020
Award Number:	DE-EE0008531
Principal Investigator:	Sameer Rao, Assistant Professor
	Phone: 801-581-4163
	Email: s.rao@utah.edu
Business Contact:	Laurel Duncan, Sponsored Projects Officer
	Phone: 801-581-3006
	Email: laurel.duncan@osp.utah.edu
Technology Manager:	Mark Lausten
Project Officer:	Christine Bing
Grant Specialist:	Patricia Clark
Contracting Officer:	Pamela Brodie

Acknowledgment: This material is based upon work supported by the Department of Energy, Office of Energy Efficiency and Renewable Energy, Solar Energy Technologies Office, Tech to Market Sub-program, under Award Number DE-EE0008531.

Executive Summary: This project seeks to exploit volumetric absorption of concentrated solar irradiation in a thin, high-temperature, thermally conductive medium. High efficiency thermal conversion is achieved by volumetric absorption of both incoming solar irradiation (short wavelength) and emitted irradiation (long wavelength), demonstrating a volumetrically absorbing thermally insulating (VATI) effect. The thermalized energy is conducted to the back wall, enclosing the working fluid (molten salt or supercritical CO_2). Reliance on conductive thermal transport requires a thermally conductive medium, in the absence of which large temperature gradients drive losses due to emission. The project's outcomes are important to realize a cost-effective approach to reduce optical and thermal losses from CSP receivers at high temperatures (720°C).

High-temperature stable and commercially available porous SiC structures (open-cell foams) were explored as a volumetrically absorbing and thermally insulating layer. To the best of our knowledge, the current state-of-the-art for industrially deployed coatings is Pyromark. However, Pyromark suffers degradation at 700+°C and diurnal temperature changes. This necessitates periodic recoating, and the downtime increases the overall levelized cost of energy (LCOE) production. On the other hand, contemporary research activities have generated significant advances in the development of selective emitter coatings, which present challenges with costs, scalability, and stability. The pursued approach alleviates these concerns by developing a receiver that utilizes the inherent structure of high-temperature stable porous materials to enable robust and cost-effective receivers which require no periodic maintenance downtimes.

The overall goal of the project is to experimentally demonstrate a figure of merit (FOM) of 0.92 at a temperature of 720°C and solar irradiation of 1000x concentration with porous receivers. The relevant crystallographic (phase) optical and thermal properties of porous SiC were first characterized. Second, the 3-D geometry of the porous SiC was analyzed using micro-X-ray tomography and converted to CAD data using image processing analysis. Utilizing this 3-D geometry and relevant optical/thermal properties, Monte Carlo-Ray Tracing (MCRT) analysis was performed to extract important parameters governing solar-thermal energy conversion such as extinction coefficient (β, 1/m), scattering albedo (ω) and the scattering phase function (Φ). These properties were then integrated into an in-house radiative and conduction transport model to solve for temperature and transport fluxes characterizing the solar-thermal energy conversion. This model was utilized to predict the FOM for various SiC porous geometries and to identify the highest possible FOM. Testing of the optimized porous structures will be accomplished with a custom-built high-accuracy (< ±4%) FOM measurement test-stand and a 1000x solar concentrator. When neglecting convective losses and resistance at the open boundary and the back wall, the optimized SiC foam leads to a FOM of 0.84. This FOM does not surpass the performance of Pyromark 2500. Yet, conversely to Pyromark 2500, SiC is stable at high temperatures and does not degrade over time. Also, it is possible to boost the FOM of SiC by engineering its effective thermal conductivity and its scattering albedo. A FOM of 0.92 is predicted for an optimized foam by accounting for convective losses and resistance at the open boundary and the back wall. This largely exceeds the FOM of Pyromark 2500 (~0.86) predicted by neglecting convective losses and resistance. Therefore, further engineering of the foam could lead to unprecedented FOMs.

Table of Contents:

Background

Contemporary solar-thermal receivers rely on absorption of solar irradiation on solid surfaces (solid at the macroscopic scale of the receiver). Volumetric receivers have been only explored for CSP applications, where an air stream is heated as it flows through – a paradigm that is distinctly different than current Gen3 CSP technologies. The investigated approach is distinctly novel, wherein incoming solar irradiation is thermalized and conducted across the back-wall to the working fluid. Radiative-conductive coupling in the foam is modeled with the radiative transfer equation (RTE) and Fourier's law.

Pyromark 2500 is the state-of-the-art coating for CSP receivers. Pyromark 2500 lacks spectral selectivity[1], which can lead to significant emission losses for concentration factor less than 500x. Most importantly, the absorptivity of Pyromark 2500 degrades substantially over time at high temperatures[1]. Spectrally selective coatings made of metallic nanoparticles in a dielectric matrix, called cermet or pigmented coatings, have been proposed for high-temperature CSP receivers [2]–[5]. Despite promising predicted and measured FOMs of respectively ~0.94 and 0.90 at for concentration factor and temperature of respectively 1000x and 750ºC [5], these coatings suffer from poor mechanical stability (delamination) at high temperature. To circumvent these limitations, we proposed robust and low-cost high-temperature porous receivers. The concept relies on converting solar irradiation into thermal energy (thermalization) within the foam and conducting the thermal energy towards the back wall separating the foam from the working fluid. For predicting the FOM of porous receivers, we developed a comprehensive framework consisting of two models:

1. Monte Carlo-Ray Tracing (MCRT): MCRT simulations have been performed to determine the foam effective radiative properties (extinction coefficient, scattering albedo, scattering phase function). We used the commercial software TracePro to perform MCRT simulations. In post-processing, we used the technique proposed by Petrash et al. [6] to retrieve the foam extinction coefficient, scattering albedo, and scattering phase function from MCRT results.

2. Coupled radiation-conduction model: The effective radiative properties obtained from MCRT simulations served as inputs to the Radiative Transfer Equation (RTE). When modeling radiation transport with the RTE, the foam is assumed to be effectively homogeneous. Various works have been devoted to solving the RTE in porous media with [7] and without [8], [9] coupling with conduction heat transfer. We used the well-established discrete ordinates method for solving the RTE and verified our model against a variety of exact results.

The framework developed during the project is comprehensive. We used the framework to predict the FOM of porous receivers, but it can also be easily applied to other structures such as flat receivers and cermet. In addition, our framework enables quantifying the impact of convective losses and resistance on the FOM. This is an important distinction with respect to the state-of-the-art in CSP receiver design, where the FOM is typically calculated based solely on spectral radiative properties without consideration of other heat losses. We also implemented an optimization procedure based on a genetic algorithm that enable determining the foam effective radiative properties and thermal conductivity [10] maximizing the FOM. Again, this is a unique contribution to CSP receiver design.

Project Objectives

The proposed VATI foam concept presents a significant departure from the typically adopted strategy in CSP research and development to engineer the spectral characteristics of the receiver material. Instead of relying on the separation of the absorption and the emission bands of the material, our approach relies on the use of the geometry of the volumetric receiver to first maximize solar absorption and secondly reabsorb the emitted radiation. Also, the porous absorber presents a significantly lower surface area in contact with the atmosphere, minimizing convective heat losses. We have already shown that despite native SiC having an absorptivity of ~0.7, the overall FOM of the VATI foam is ~0.87 (comparable to Pyromark with an absorptivity of 0.93). SiC foam is commercially available globally and comprised of earth-abundant materials. In terms of operational characteristics, the off-the-shelf SiC foam can offer comparable performance to Pyromark 2500 and does not need to be recoated. SiC is a high-temperature stable material and does not degrade in the ambient. Considering these salient features, we expect that SiC VATI foam can be widely integrated into commercial CSP plants, enabling low levelized costs of electrical energy from CSP. Achieving high receiver efficiency is critical to reducing the overall SunShot 2030 CSP goal of $0.05/kWh. In addition, the fundamental understanding of volumetric absorption of concentrated sunlight and coupled thermal transport at high temperatures in porous structures has significant gaps in the contemporary scientific literature. In fact, the design and optimization of the VATI foam would not be possible without the knowledge generated by this project. In order to accomplish the project objective, we have focused on the following three tasks:

Task 1 was defined to characterize the VATI foam and develop detailed models for multi-mode thermal transport – ultimately enabling the optimization of structural parameters to achieve the desired optical and thermal performance.

Task 2 focused on the development of a testing platform that can directly measure the FOM at elevated temperatures (~750 ºC) in vacuum and ambient conditions (*i.e.*, with and without convective heat loss).

Task 3 pertains to the design and construction of the concentrated solar simulator. Outcomes from Tasks 2 and 3 will enable the experimental testing of the optimized foam geometry in realistic operation conditions: solar irradiation of 1000x (100 W/cm^2) and temperature > 750 ºC.

The milestones and achieved outcomes for each task are described below:

M1.1.1: Characterization of pore size and porosity of commercial SiC foam

Outcome: Technique developed to analyze foams with micro-CT and extract pore characteristics (full 3-D CAD representation, pore size, and its distribution, average and local porosity).

M1.1.2: Characterization of relevant optical properties of SiC

Outcome: X-ray diffraction was performed on CVD SiC by the SiC vendor. Phase identified as 3C. Optical properties (input for subsequent calculations) extracted from literature, ellipsometry, and first principles.

M1.2.1 and M1.2.2: Optimized geometry and structure of VATI foam for Pyromark and metal oxide back walls, respectively

Outcome: Design of SiC foam with predicted FOM of ~0.84 achieved. This result was achieved with off-the-shelf SiC foam, and optimization indicates that FOM of 0.92 is feasible with favorable optical properties.

M1.3.1: VATI foam performance (experimental)

Outcome: SiC foam with optimum properties manufactured. High-temperature brazing to join SiC foam to the tungsten reference bar was successfully developed.

This task was unable to be completed during the performance period.

Experimental testing of VATI foams will be continued outside the scope of the current award. Generated results will be disseminated in leading academic journals.

M2.1.1: Heat flux meter cooling

Outcome: Temperature drop in the bar was designed to enable heat rejection at ~100°C, and heat rejection heat flux was reduced by spreading the heat through a 4x larger footprint. Reference bar fabrication was also completed.

M2.1.2: Operation of high-temperature heat flux meter

Outcome: Pyromark 2500 was chosen to serve as a benchmark for the FOM measurement apparatus. However, the performance team was unable to develop a stable coating of Pyromark 2500 on tungsten. An alternative benchmark solar receiver coating in oxidized Inconel-625 was explored and deemed suitable as a benchmark.

This task was unable to be completed during the performance period.

Experimental performance of the reference bar technique will be continued outside of the scope of DOE award. Generated results will be disseminated in leading academic journals.

M2.2.1: Test chamber operation for high temperature FOM measurement

Outcome: Chamber designed, constructed, and integrated successfully with the reference bar and solar simulator.

M3.1.1: Design of elliptical reflector geometry and lamp housing

Outcome: Reflector and lamp housing design completed to operate with vacuum chamber and reference bar assembly. 1000X concentration across 1-in. diameter circular cross-sectional area achieved.

M3.1.2: Testing of the concentrated solar simulator

Outcome: Calibration completed - successfully matching program requirements.

Project Results and Discussion

Task 1: Development, characterization, and optimization of VATI foam

Summary: When neglecting convective losses and resistance at the open boundary and the back wall, as done in the literature, the optimized SiC foam leads to a FOM of 0.83. This FOM does not surpass the performance of Pyromark 2500. Yet, conversely to Pyromark 2500, SiC is stable at high temperatures and does not degrade over time. Finally, it is possible to boost the FOM of SiC by engineering its effective thermal conductivity and its scattering albedo. Indeed, an FOM of 0.92 is predicted by accounting for convective losses and resistance at the open boundary and the back wall. This largely exceeds the FOM of Pyromark 2500 (0.86) predicted by neglecting convective losses and resistance. Therefore, further engineering of the foam could lead to unprecedented FOMs.

Sub-task 1.1: Characterize foam pore size and optical properties of silicon carbide (SiC)

Milestone 1.1.1: Characterization of pore size and porosity of commercial SiC foam

Milestone 1.1.1 status: Completed 100% as of 09/15/2019. Pore size (200 ± 25 μm) and porosity (0.80 ± 0.02) successfully measured. Statistical variations analyzed. 3D model generated as an input for MCRT.

Milestone 1.1.1 is focused on the direct measurement of geometrical properties of the commercial samples of SiC foam obtained from ERG Aerospace. The porosity of SiC foams from ERG Aerospace was derived from μCT data. First, a cylindrical SiC foam sample (diameter = 2 cm, thickness = 6 mm, porosity = 0.85) was scanned in the μCT instrument at the UoU. This resulted in 300 2D images having a resolution of 1012 x 1024

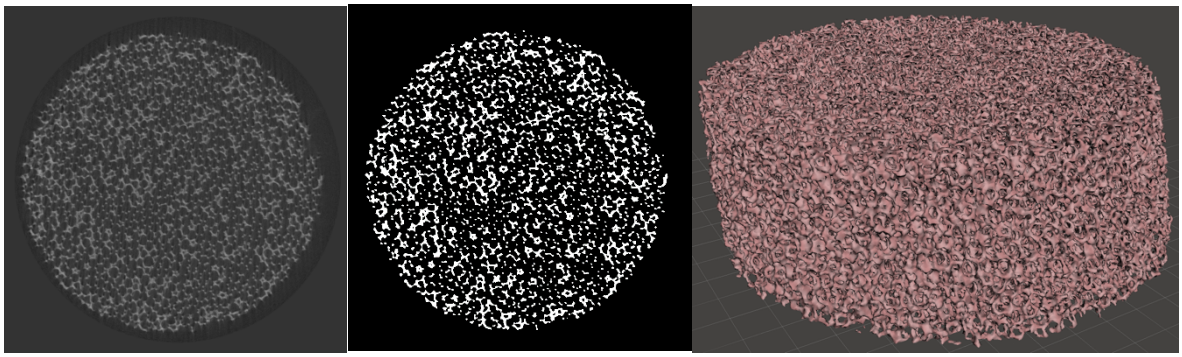

(a) (b) (c)

Figure 1: μCT scan of the SiC foam: (a) 2D image. (b) 2D binarized image. (c) 3D foam.

pixels. Each pixel corresponds to a cube having a side length of 19.32 μm. Figure 1(a) shows an image obtained from μCT. Next, the software Fiji was used to binarize the images and smooth out the ligaments to remove the noise (see Fig. 1(b) for example of binarized image). Finally, the 2D binarized images were converted into a 3D surface mesh via the module BoneJ in Fiji. Figure 1(c) shows the reconstructed 3D foam.

For characterizing the porous characteristics of the foam, the binary μCT images were then exported into a 3D visualization and analysis software. Based on intensity thresholding and a cuboidal analysis volume, the phases were discriminated against, i.e., the solid elements and the voids were labeled as discrete entities (Fig. 2). The volume occupied by each phase was then calculated from the parent scale and size of the entire foam. The volume fraction for each phase can then be calculated. This analysis was performed for 10 cuboidal elements chosen at random. These replicate measurements enable a null hypothesis test against the manufacturer specification. From the analysis of μCT data the porosity of the test sample was estimated to be 0.80 ± 0.02 and thus the null hypothesis was rejected. This discrepancy was discussed with the vendor and it was inferred that this error was likely a manufacturing defect. The vendor highlighted that they recently revamped their SiC foam processing line and the tested sample was from a batch where parameters were still being fine-tuned. It is important to emphasize that the deviation from the manufacturer specification on the porosity will not affect the predictions from the radiative model. This is because the μCT data is directly converted into the CAD model for predicting the foam effective radiative properties via Monte-Carlo Ray Tracing, ensuring high-accuracy predictions. In addition, the ~5% bias in porosity has a negligible impact on the effective

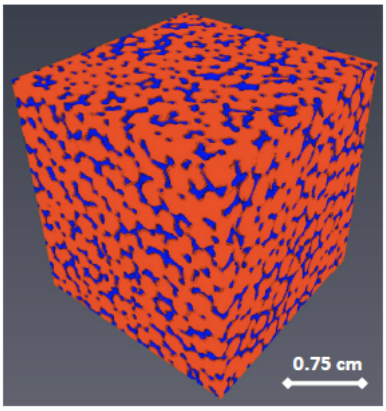

Figure 2: The μCT scan of the foam was segmented to discriminate the solid SiC phase (blue) and the void space (red). The volume was sampled at 10 random locations with a sample cell measuring 0.25 x 0.25 x 0.25 cm to enable replicate measurements.

thermal conductivity of the foam. The average diameter size d_p was estimated to be 200 $\pm$ 25 μm, which is consistent with the vendor specification.

Milestone 1.1.2: Estimate the complex refractive index of silicon carbide in foams and identify its physical phase

Milestone 1.1.2 status: Completed 100% as of 1/15/2020. Refractive index data for amorphous SiC from literature was used due to a lack of sufficient data in the literature.

Based on our experiments to measure and identify the phase of SiC in the foams, we were able to conclude that the predominant phase is cubic or 3C or b. After extensive literature data review, we conclude that the spectral optical properties were sufficiently similar to amorphous SiC. These properties were integrated into the coupled radiation-conduction transport model for all subsequent FOM predictions. There is a lack of experimental data for the 3C-SiC in literature. However, the optical properties of the 3C-SiC in the infrared range can be calculated using the Lorenz model. We have compared the properties from the Lorenz model with the optical properties available for amorphous SiC in the literature [11]. We can see a similar trend in the properties for the most part of the wavelengths.

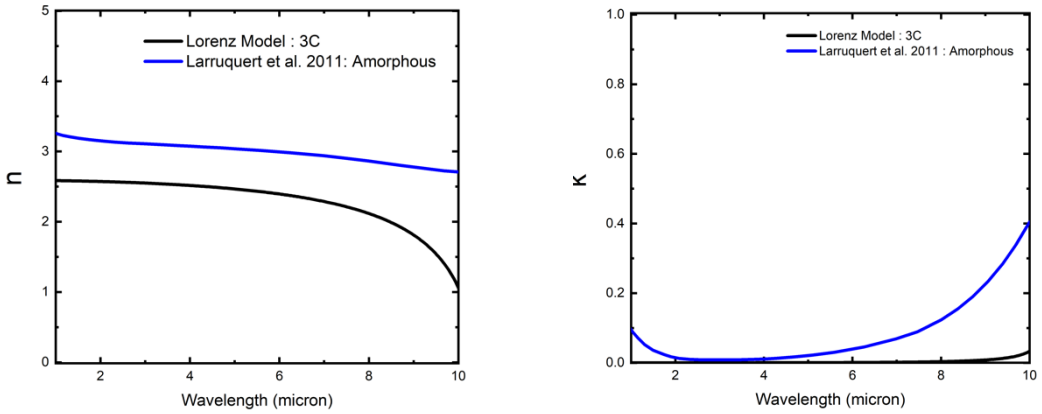

Figure 3: Comparison of optical properties for 3C SiC from the Lorenz model and amorphous SiC from literature.

As we do not have any source of optical properties for 3C-SiC for the short wavelengths, we have compared properties for other phases in this range of wavelengths. For the 4H and 6H phases of SiC, we found only the real part of the refractive index (n) from literature [12]. So, the comparison is shown only for this range. Here, we can say that the optical properties of SiC have a very small difference between phases. Therefore, we decided to use amorphous SiC properties from Ref. [11] for the entire wavelength range for our calculations.

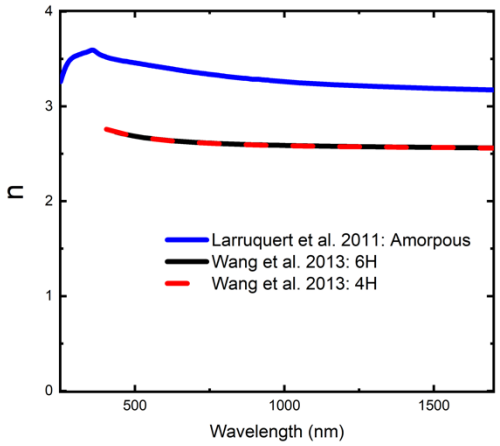

Figure 4: Comparison of optical properties for amorphous, 4H, and 6H SiC from literature.

Sub-task 1.2: Develop a computational framework and optimize VATI foam characteristics using models for coupled optical and thermal effects (Note: Results demonstrate that the FOM is nearly insensitive to the back wall; thus the results for both milestones are the same.)

Milestone 1.2.1 status: Completed 100% as of 3/1/2020. Design of SiC foam with predicted FOM of 0.81 achieved (~0.83 when convective losses are neglected). Design of optimized foam with FOM of ~0.94 achieved with idealized optical and thermal properties.

Determination of engineered optical coatings leading to higher FOM will be pursued in the future outside the scope of the current award.

Milestone 1.2.2 status: Completed 100% as of 8/1/2020. Design of SiC foam with predicted FOM of 0.81 achieved (~0.83 when convective losses are neglected). Design of optimized foam with FOM of ~0.94 achieved with idealized optical and thermal properties.

The computational framework consists of two main parts. First, a Monte-Carlo Ray Tracing (MCRT) model is used for predicting the effective radiative properties of the VATI foam. These effective radiative properties are the extinction coefficient, the scattering albedo, and the scattering phase function. Second, the effective radiative properties serve as inputs to a coupled radiation-conduction transport model combining the Radiative Transfer Equation (RTE) and Fourier's law. The figure-of-merit of the VATI foam is calculated from the coupled radiation-conduction model.

A. Monte-Carlo Ray Tracing (MCRT) framework for predicting effective radiative properties

Radiation transport in the foam is modeled via the RTE. When using the RTE, it is assumed that the foam is effectively homogeneous (i.e., effective medium theory). The impact of the optical properties of the solid phase and voids (i.e., refractive index), as well as the foam geometry (i.e., foam porosity and distribution, cellular ligament diameter), is taken into account via the effective radiative properties. The basic effective radiative properties describing the foam are the absorption coefficient, κ, and the scattering

coefficient, σ_s, which are the inverse of the absorption and scattering mean free paths, in addition to the scattering phase function, Φ. The effective radiative properties are often combined into an extinction coefficient, β, and a scattering albedo, ω, respectively defined as:

$$\beta = \kappa + \sigma_s \tag{1}$$

$$\omega = \frac{\sigma_s}{\kappa + \sigma_s} = \frac{\sigma_s}{\beta} \tag{2}$$

The effective radiative properties can be estimated via the foam porosity and the mean pore diameter using simple correlations. However, this approach does not account for the intricate foam structure. Instead, the team is using a MCRT framework in conjunction with the μCT images of the foam to determine in a precise and rigorous manner the effective radiative properties.

MCRT calculations are performed using the software TracePro. The 3D foam image obtained from Fiji (see Fig. 1(c)) is imported into TracePro after conversion into an .SAT file via the software CAD Exchanger. The optical properties of the solid foam phase can be assigned via surface properties (e.g., reflectivity calculated via the Fresnel coefficients) or via volume properties (i.e., real and imaginary parts of the refractive index). N_r rays are traced from a randomly selected origin on a surface of the solid phase along a randomly selected propagation direction until they reach another surface where they are either scattered or absorbed. The path-lengths of these rays, $s_{\mathrm{e,m}}$, define a cord length probability density function [6]:

$$F_{\mathrm{e}}(s) = \frac{1}{N_r} \sum_{\mathrm{m}=1}^{N_r} \delta\left(s - s_{\mathrm{e,m}}\right) \tag{3}$$

where δ is the Dirac delta function. The probability of a ray being extinct before reaching a distance s is therefore calculated as follows:

$$G_{\mathrm{e}}(s) = \int_0^s F_{\mathrm{e}}(s')\,ds' = \frac{1}{N_r} \sum_{\mathrm{m}=1}^{N_r} H\left(s - s_{\mathrm{e,m}}\right) \tag{4}$$

where H is the Heaviside step function. The probability of a ray being extinct before reaching a distance s can also be predicted via Beer's law:

$$G_e(s) = 1 - \exp(-\beta s) \tag{5}$$

In Eq. (5), the exponential term represents the transmitted portion of radiative intensity traveling a distance s within the foam.The term $G_e(s)$ is calculated in TracePro via Eq. (4). Then, by using Eq. (5) and the least square method, the foam extinction coefficient β is retrieved.

The number of rays that are absorbed, N_a, and scattered, N_s, are also recorded by TracePro. Using this information, the scattering albedo ω is calculated as follows:

$$\omega = \frac{N_s}{N_s + N_a} \tag{6}$$

The probability of a ray propagating along a direction μ' to be scattered in a direction μ is described by the scattering phase function $\Phi(\Theta)$. The angle between the incident and the scattered directions defines Θ, and the scattering phase function is calculated as:

$$\Phi(\Theta) = \frac{W(\Theta)}{\frac{1}{4\pi}\int_{4\pi} W(\Theta)\, d\Omega} \tag{7}$$

where $W(\Theta)$ is the distribution function of scattering directions of the rays traced in TracePro.

B. Effective radiative properties of the SiC foam

In order to verify the accuracy of the MCRT framework described in section A, simulations have been performed on a simplified test foam made of 3000 faces (see Fig. 3(a)). The test foam is characterized by a porosity of 80% and a mean pore diameter of 4.26 mm. It is also assumed that the solid phase is made of SiC as for the actual foam.

The extinction coefficient of the test foam was first estimated via the correlation proposed by Hendricks and Howell [13]:

$$\beta = \Psi \frac{1-\phi}{d_p} \tag{8}$$

where ϕ is the foam porosity, d_p is the mean pore diameter, while Ψ is a constant that depends on the material constituting the foam solid phase. For SiC, a Ψ value of 4.8 is recommended. Using Eq. (8), the extinction coefficient β of the SiC test foam is estimated to be 225 m^{-1}.

The effective radiative properties of the SiC test foam were then calculated using the MCRT framework. It was determined that a total number of 100,000 rays is sufficient to obtain stable and converged results. The predicted effective radiative properties of the SiC test foam for wavelengths of 1 μm and 3.5 μm are provided in Table 1.

Table 1: Effective radiative properties of the SiC test foam calculated via MCRT as implemented in TracePro.

Wavelength λ (μm)	**Properties**	**Extinction coefficient β (m^{-1})**	**Scattering albedo ω (-)**
1	Surface	272	0.311
	Volume	272	0.306
3.5	Surface	271	0.294
	Volume	273	0.291

The extinction coefficient predicted by MCRT is in reasonable agreement with the estimation provided by Hendricks and Howell's correlation (Eq. (8)). The discrepancies are due to the fact that the correlation does not account for the actual foam geometry, and due to the fact that the SiC optical properties are taken into account via an effective

parameter Ψ. Also, it is clear from Table 1 that the effective radiative properties are unaffected by the way the properties are assigned in TracePro (surface versus volume). The results shown in Table 1 have been generated using both uniform and Lambertian emission sources. It was concluded that the effective radiative properties are not affected by the angular distribution of the emission source. From the simulations performed with the test foam, the team concluded that the MCRT method implemented in TracePro provides accurate results, and can thus be used for predicting the effective radiative properties of the actual SiC foam.

For the actual SiC foam, the 3D image shown in Fig. 1(c) is very large compared to the mean pore diameter of ~ 200 μm. Such a large representation of the SiC foam is not necessary to obtain accurate effective radiative properties from MCRT simulations. Indeed, the only condition imposed by the MCRT method is to perform the simulations on a geometry representative of the actual foam that is large enough to neglect side effects. For example, Fig. 5(b) shows a smaller portion of the SiC foam characterized by a diameter and a thickness of respectively 3 mm and 2 mm. Even for this smaller geometry, MCRT simulations need significant amount of computational resource since the solid phase of the foam must be discretized into 50,000 faces to represent accurately the actual geometry.

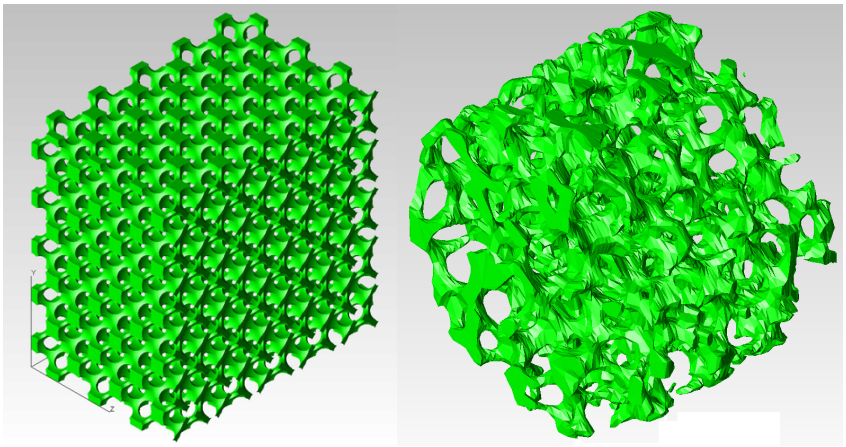

(a) (b)

Figure 5: (a) Test foam used for verifying the accuracy of MCRT simulations. (b) Representative part of the SiC foam suitable for MCRT simulations.

MCRT simulations on the actual SiC foam resulted in an extinction coefficient β of 2440 m^{-1}. Note that the extinction coefficient is not a function of the wavelength, and only depends on the foam structure. This value is in reasonable agreement with the estimation of 3600 m^{-1} provided by Hendricks and Howell's correlation (Eq. (8)).

The SiC foam scattering albedo ω is a function of the wavelength as the proportion of scattering to the overall extinction in the foam depends on the optical properties of SiC, which in turn depend on the wavelength. Figure 6 shows the scattering albedo predicted via MCRT simulations, where it is observed that scattering is the largest at short wavelengths.

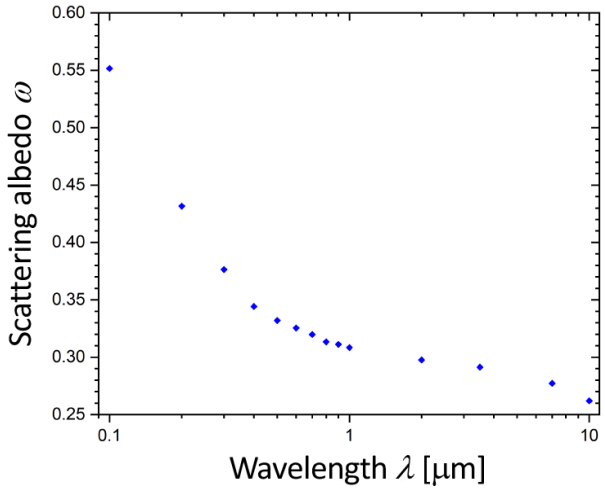

Figure 6: Scattering albedo of the actual SiC foam calculated via MCRT.

Finally, the scattering phase predicted with MCRT, shown in Fig. 7, reveals that the SiC foam leads to anisotropic scattering. This result is in reasonable agreement with the scattering phase function reported by Coquard et al. [8].

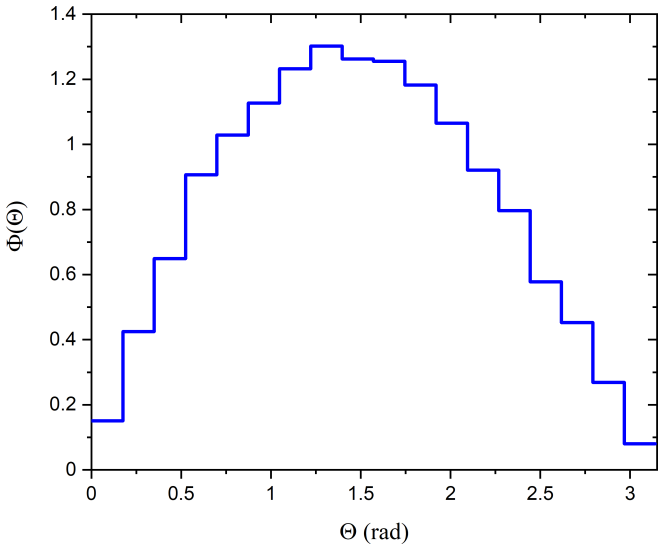

Figure 7: Scattering phase function of the SiC foam calculated via MCRT.

C. Coupled radiation-conduction model for predicting the FOM

A schematic representation of the one-dimensional radiation-conduction transport model is shown in Fig. 8.

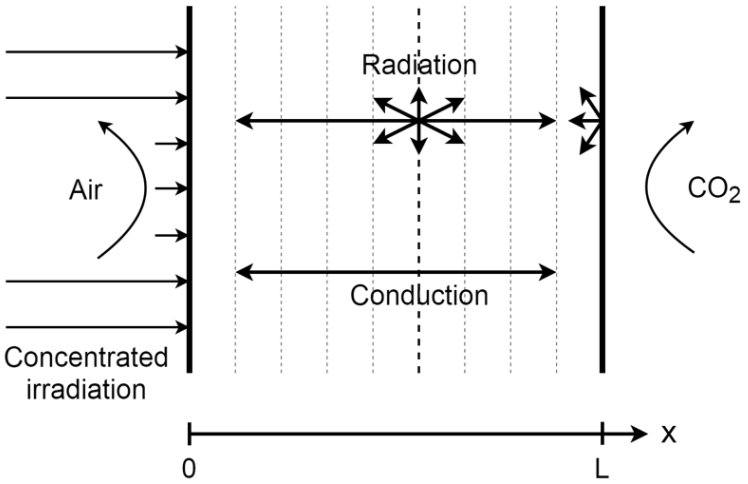

Figure 8: Schematic of the radiation-conduction model used for predicting the FOM. The geometry is one-dimensional as the foam thickness, *L*, is much smaller than its diameter. Radiation and conduction transport within the foam are modeled via the RTE and Fourier's law, and are coupled to each other via the energy equation.

The RTE is used to model radiation transport in the foam. The RTE describes the spatial variation of intensity inside the foam along a specific direction $\mu = \cos\theta$, where θ is the polar angle defined with respect to the *x*-axis (azimuthal symmetry is assumed). When dealing with solar irradiation, it is best to split the radiative intensity *I* in two parts, namely a collimated component, I_c, and a diffuse component, I_d. Note that in all equations shown hereafter, it is implicitly assumed that the intensity and radiative properties depend on the wavelength λ.

Concentrated solar irradiation incident on the foam open boundary ($x = 0$) is modeled as a collimated intensity, I_c:

$$I_c(0) = Cq''_{sol}\delta(\mu - \mu_{sol}) \tag{9}$$

where q''_{sol} is the solar radiative flux (0.1 W/cm^2), *C* is the concentration factor, whereas $\mu_{sol} = \cos\theta_{sol}$ is the direction cosine of the solar irradiation. At normal incidence, $\theta_{sol} = 0^o$ such that the direction cosine $\mu_{sol} = 1$.

The spatial variations of the solar irradiation penetrating the VATI foam are calculated in an exact manner via Beer's law:

$$I_c(\tau) = I_c(0)\exp(-\tau) \tag{10}$$

where $I_c(0)$ is the incident solar irradiation given by Eq. (9). The optical depth is defined as $\tau = \beta x$. Physically, Eq. (10) implies that solar irradiation is exponentially attenuated along its path within the foam due to absorption and scattering.

The solar irradiation scattered in the foam is described by a diffuse intensity, I_d. The RTE is used to model the spatial variations of diffuse intensity within the foam along a specific direction $\mu = \cos\theta$ as follows:

$$\frac{\partial I_d(\tau,\mu)}{\partial \tau} = -I_d(\tau,\mu) + (1-\omega) I_b(T,\tau,\mu) + \frac{\omega}{4\pi}\int_{4\pi} I_d(\tau,\mu')\Phi(\mu',\mu)d\mu' + S_c(\tau,\mu) \quad (11)$$

where I_b is the spectral blackbody intensity, and $\Phi(\mu',\mu)$ is the scattering phase function providing the probability that radiation propagating along the direction μ' is scattered along the direction μ. The term S_c is a source function that accounts for the solar irradiation converted into diffuse intensity, I_d, due to scattering within the foam:

$$S_c(\tau,\mu) = \frac{\omega}{4\pi} I_c(\tau)\Phi(\mu_{sol},\mu) \quad (12)$$

The open boundary ($x = 0$) is assumed to be transparent to solar irradiation because there is no solid wall. Yet, radiation can leave by the open boundary due to backscattering by the foam. At the back wall ($x = L$), the boundary is assumed to be emitting, absorbing and reflecting. The amount of emission, absorption and reflection depends on the radiative properties of the back wall.

The solar irradiation absorbed by the foam is converted into thermal energy. Transport of thermal energy by conduction within the foam is calculated via Fourier's law. Convection heat transfer in the foam is neglected. Conduction heat transfer affects the temperature distribution within the foam, which in turns affects thermal emission by the foam (modeled via the spectral blackbody intensity I_b in Eq. (11)). Radiation and conduction transport in the foam are coupled with each other via the energy equation:

$$\nabla\cdot(\mathbf{q}_r'' + \mathbf{q}_c'') = 0 \quad (13)$$

where $\mathbf{q}_r''$ and $\mathbf{q}_c''$ are the radiation and conduction flux vectors. The divergence of the radiative flux vector is calculated from the diffuse and collimated intensities as follows:

$$\nabla\cdot\mathbf{q}_r'' = 2\pi\kappa\left(2I_b(T,\tau,\mu) - \int_{-1}^{1} I_d(\tau,\mu)d\mu - \frac{I_c(\tau)}{2\pi}\right) \quad (14)$$

where κ is the foam absorption coefficient. Inserting Fourier's law and Eq. (14) into Eq. (13), the energy equation can then be written as:

$$k\nabla^2 T = 2\pi\kappa\left(2I_b(T,\tau,\mu) - \int_{-1}^{1} I_d(\tau,\mu)d\mu - \frac{I_c(\tau)}{2\pi}\right) \quad (15)$$

where k is the effective thermal conductivity of the foam. Convection heat transfer in air and supercritical CO_2 are respectively modeled at the open boundary ($x = 0$) and the back wall ($x = L$).

The FOM is calculated as the ratio of the heat flux transferred to the supercritical CO_2 at the back wall, $q''_{converted}$, over the incident solar irradiation:

$$\mathrm{FOM} = \frac{q''_{converted}}{Cq''_{sol}} \quad (16)$$

A finite-difference approach is used for solving the energy equation. The discrete ordinates method (DOM) is employed for solving the RTE, where the angular integral is

replaced by a numerical quadrature. In the DOM, the angular domain of 4π sr is discretized into *M* directions, such that *M* RTEs are solved. The *M* RTEs are coupled with each other via the spectral blackbody intensity and the in-scattering term (i.e., integral term in Eq. (11)). The energy equation and RTEs are solved iteratively, as the diffuse intensity is a function of the temperature distribution within the foam, while the temperature distribution in the foam depends on the spatial distribution of diffuse and collimated intensities.

The radiation transport model has been verified against various exact results. Figure 9 shows a sample result for radiation transport with collimated irradiation in a purely scattering medium ($\omega = 1$). The non-dimensional radiative heat flux is plotted against the optical thickness of the medium, τ_L (= βL, where *L* is the actual thickness of the medium), and the angle of incidence, μ_0, of the collimated irradiation. The results obtained from the DOM are compared against exact results (Modest, *Radiative Heat Transfer*, Chapter 19, p. 616, Third Edition, Academic Press, 2013, [14]). It is clear from Fig. 9 that the radiation transport model with collimated irradiation provides accurate results. The team concluded that the radiation-conduction transport model can be confidently applied for predicting the FOM of the actual SiC foam.

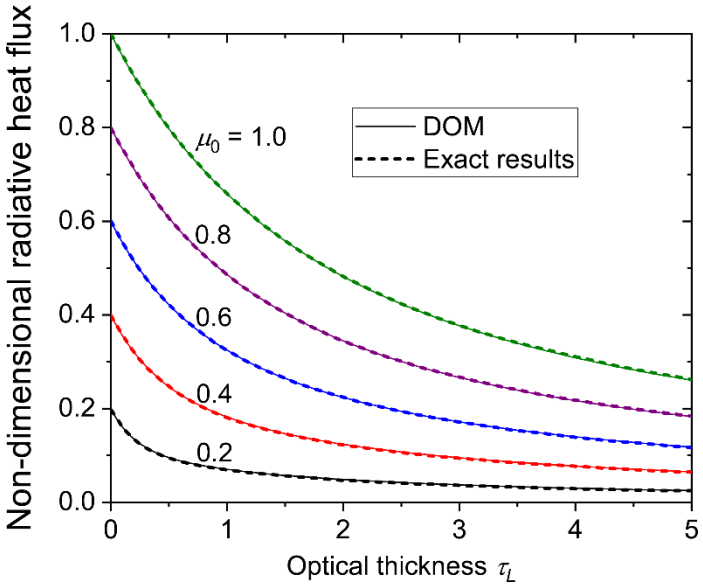

Figure 9: Non-dimensional radiative heat flux in a purely scattering medium with collimated irradiation. DOM simulations are compared against exact results.

D. FOM of SiC foam

The FOM of the SiC foam characterized in sections A and B is predicted via the coupled radiation-conduction model. The foam has a porosity ϕ of 0.85 and an average pore diameter d_p of 200 μm. The frequency-independent extinction coefficient β of the foam is 2440 m^{-1}. The scattering albedo and scattering phase function are provided in Figs. 6 and 7, respectively.

A heat transfer coefficient of 10 W/m^2K and a surrounding air temperature of 300 K are used at $x = 0$ (open boundary), while a heat transfer coefficient of 18,000 W/m^2K and a supercritical CO_2 temperature of 1000 K are assigned at $x = L$ (back wall). Solar irradiation

is at normal incidence (μ_{sol} = 1) with a concentration factor C of 1000. Coupled radiation-conduction transport in the SiC foam is calculated by assuming that the back wall is made of SiC characterized by a wavelength-dependent emissivity predicted via fluctuational electrodynamics (see Fig. 10). The effective thermal conductivity k_{eff} of the foam is calculated from the porosity ϕ and the temperature-dependent bulk thermal conductivity k_b of SiC (see Fig. 9) using the correlation of Bracconi et al. [10]:

$$\frac{k_{eff}}{k_b} = \frac{1-\phi}{\left(\frac{2}{3}(1-\phi)+\frac{1}{3}\right)^{-1}} \tag{17}$$

Note that the effective thermal conductivity depends on the foam temperature since the temperature-dependence of the SiC bulk thermal conductivity is considered.

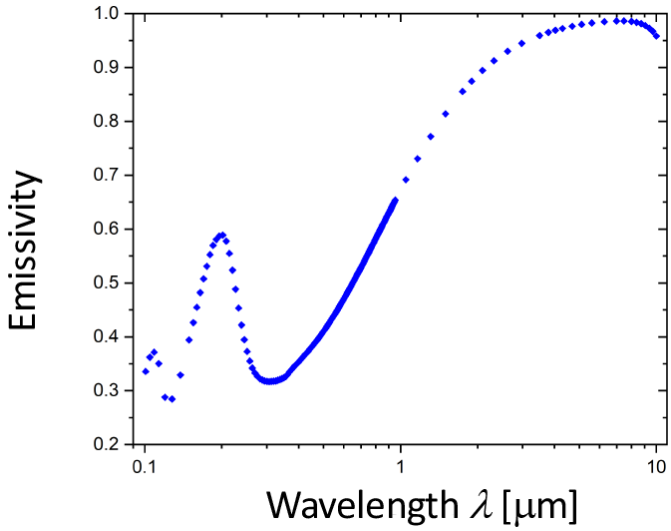

Figure 10: Emissivity of the SiC back wall as a function of the wavelength λ.

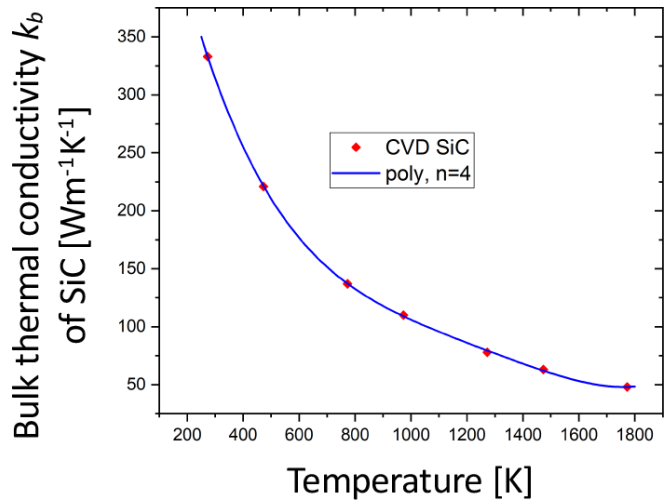

Figure 11: Bulk thermal conductivity k_b of SiC as a function of the temperature.

For a 1-mm-thick SiC foam, an FOM of 80.64% is predicted via the radiation-conduction model. The temperature distribution and the nondimensional heat flux distributions are shown in Fig. 12. The flux distributions are normalized by the total incident collimated solar irradiation flux (10^6 Wm^{-2}).

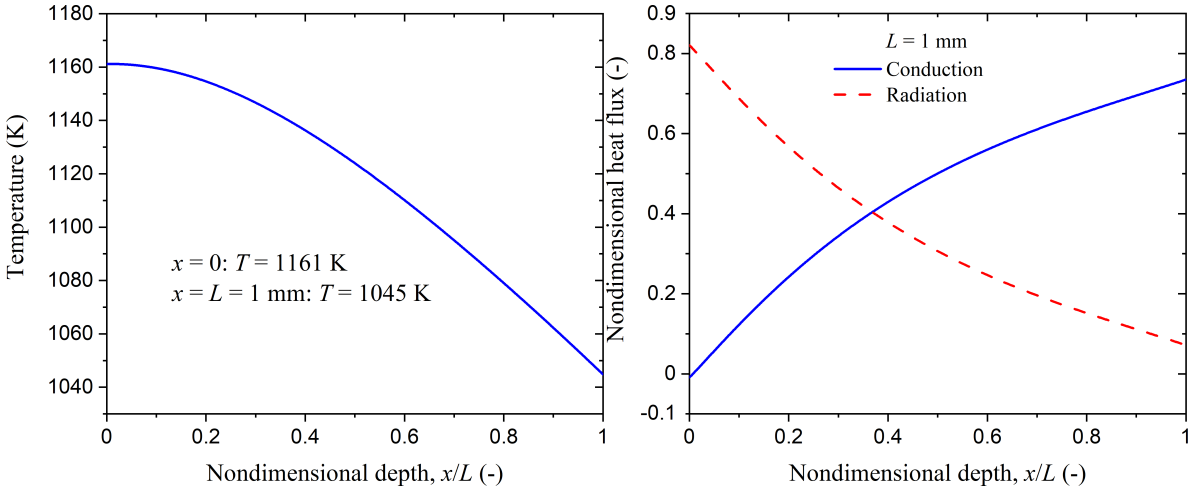

Figure 12: Temperature and nondimensional flux distributions in the 1-mm-thick SiC foam.

Our concept for maximizing the FOM relies on converting the solar irradiation into thermal energy within the foam (see Fig. 12). In that way, conduction is the main mechanism by which thermal energy is transported to the back wall, such that the radiative properties of the back wall have a low impact on the FOM. Therefore, the low thermal conductivity of the SiC foam (2.97-3.43 $Wm^{-1}K^{-1}$) is one of the key limiting factors to the FOM.

Note that in the limiting case that there is no foam (i.e., only a back wall of SiC absorbs solar irradiation), the FOM can be estimated as follows:

$$\mathrm{FOM} = \frac{\alpha C q''_{sol} - \varepsilon \sigma T^4}{C q''_{sol}} \tag{18}$$

Using a back wall temperature of 1045 K as predicted via the coupled radiation-conduction model, the FOM is estimated to be 50.6%. Therefore, it is clear that the foam significantly increases the FOM when compared to the case of a flat receiver. Here, the FOM is enhanced by ~30% owing to the presence of the 1-mm-thick SiC foam.

It is advantageous to have a foam with large enough optical thickness τ_L enabling most of the solar irradiation to be extinct in the foam. As shown Fig. 12, an optical thickness of τ_L = 2.44 results in a small radiative flux at the back wall since most of the solar irradiation is thermalized by the foam. The conduction thermal resistance is directly proportional to the foam thickness, while it is inversely proportional to the effective thermal conductivity of the foam. For a fixed optical thickness, the conduction thermal resistance decreases

by reducing the foam thickness L, which results in an increase of the extinction coefficient β. A large β-value leads to a large absorption of the solar irradiation close to the open boundary ($x = 0$). This however negatively affects the FOM since the radiative heat losses from the foam to the air increases. A decrease of the extinction coefficient β results in a smoother decay of the solar irradiation in the foam. Yet, this causes an increase in the conduction thermal resistance as the thickness of the foam increases. In all cases, the FOM is negatively impacted by reducing β. Therefore, there is an optimal combination of β and L that maximizes the FOM of the SiC foam.

The sensitivity of the SiC foam to the thickness L and extinction coefficient β is analyzed hereafter. In one case, the SiC foam has an extinction coefficient fixed at 2440 m^{-1} and a variable thickness. In the other case, the SiC foam has a fixed thickness of 1 mm and a variable extinction coefficient. The results are shown in Fig. 13.

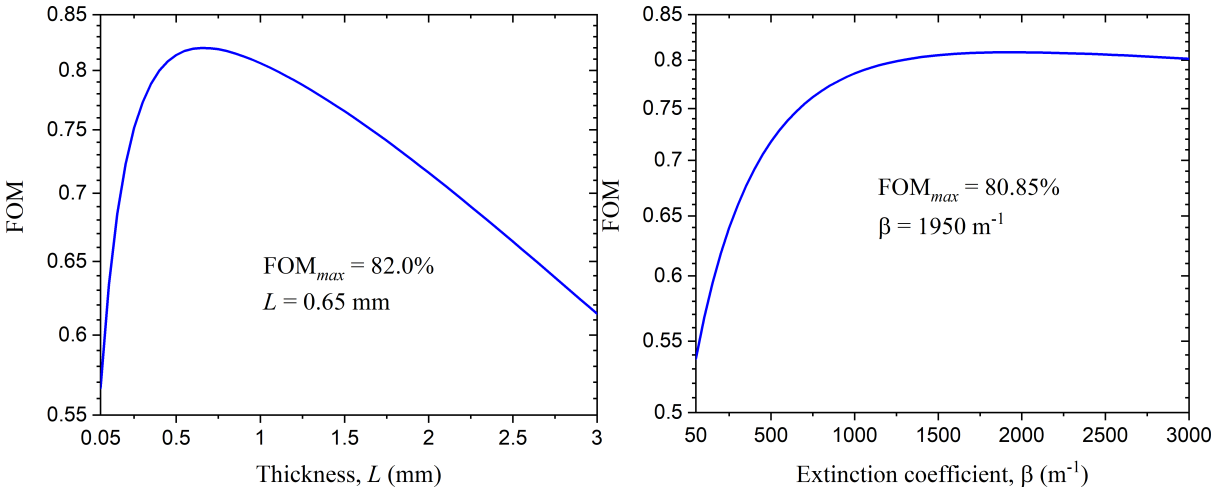

Figure 13: Sensitivity of the FOM of the SiC foam to the thickness L for an extinction coefficient of 2440 m^{-1} (left panel) and to the extinction coefficient β for a fixed thickness of 1 mm.

A maximum FOM of 82% is predicted for an SiC foam with an extinction coefficient of 2440 m^{-1} and a thickness of 0.65 mm. These results support that there is an optimal combination of extinction coefficient and sample thickness that maximizes the FOM.

In the next section, a foam maximizing the FOM is designed via a genetic algorithm.

E. Design of foam maximizing the FOM

A genetic algorithm (GA) is used to design an SiC foam maximizing the FOM. Specifically, the foam thickness L and extinction coefficient β are the variable input parameters in the GA that are respectively allowed to vary between 1 and 3 mm and between 1200 and 3500 m^{-1}. The fixed input parameters are the scattering albedo of the SiC foam (see Fig. 4) and the emissivity of the SiC back wall (see Fig. 11), in addition to the average pore diameter d_p of 200 μm. In the GA simulations, the foam porosity ϕ required to calculate the effective thermal conductivity is estimated from the extinction coefficient and the average pore diameter via the correlation of Hendricks and Howell (Eq. (8))[13].

The optimized SiC foam, as determined by the GA, has a maximum FOM of 80.7% and is characterized by the following parameters: β = 1858 m^{-1}, L = 1.02 mm, ϕ = 0.923 and k_{eff} = 2.60-3.02 $Wm^{-1}K^{-1}$. Here, the maximum FOM is lower than that reported in section D since the minimum foam thickness is limited to 1 mm. We would like to emphasize that all FOM values are calculated by assuming convective losses at the open boundary (T_{air} = 300 K, h_{air} = 10 $Wm^{-2}K^{-1}$) and a convective resistance at the back wall (T_{CO2} = 1000 K, h_{CO2} = 18,000 $Wm^{-2}K^{-1}$). These parameters were selected in order to predict realistic, physically meaningful FOM values. However, FOMs reported in the literature do not account for convective losses and resistance. When convective losses and resistance are neglected at the open boundary and back wall, the FOM of the optimized SiC foam increases to a value of 83.4%. This FOM value of 83.4%, instead of 80.7%, should be compared against the FOMs reported in the literature.

The FOM can be further increased via two approaches. First, since our concept relies on conducting thermalized radiation towards the back wall, the foam effective thermal conductivity affects significantly the FOM. Fig. 14(a) shows the FOM of the optimized SiC foam as a function of k_{eff}, while Fig. 14(b) provides the sensitivity of the FOM to k_{eff}. Here, it is assumed that it is possible to engineer the effective thermal conductivity of the SiC foam independently of its porosity.

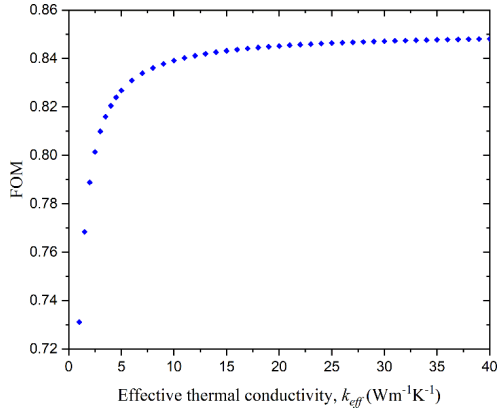

(a)

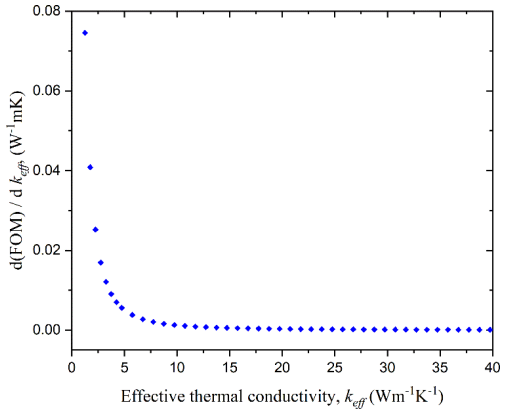

(b)

Figure 14: (a) FOM as a function of the effective thermal conductivity k_{eff} for the optimized SiC foam. (b) Sensitivity of the FOM to k_{eff}.

Increasing k_{eff} to a value of ~ 10 $Wm^{-1}K^{-1}$ enhances the FOM of the optimized SiC foam to ~ 84%. This is a significant gain of ~ 3-4%. It is clear from Fig. 14(b) that increasing k_{eff} beyond 10 $Wm^{-1}K^{-1}$ does not have any perceptible impact on the FOM.

The second approach for increasing the FOM is to change the radiative properties of the foam, by either using a different material than SiC or by coating the SiC foam. To quantify the possible gain in FOM when varying the foam radiative properties, GA simulations are performed by adding a variable input parameter, namely the foam scattering albedo ω. The scattering albedo is a dimensionless variable, taking values between 0 and 1, quantifying the amount of scattering with respect to the total extinction. Specifically, the scattering albedo is allowed to take two different values within two distinct spectral bands. The cutoff wavelength at which the value of the scattering albedo changes is also determined via the GA. We verified that discretizing the scattering albedo in more than two spectral bands did not affect the results. Figure 15 shows the FOM for foams with optimized scattering albedo as a function of the effective thermal conductivity. Case 1 involves a SiC back wall, while the emissivity ε_w of the back wall is optimized in case 2. Every point in Fig. 15 has been optimized via the GA; the foam properties for all points are provided in Tables 2 and 3.

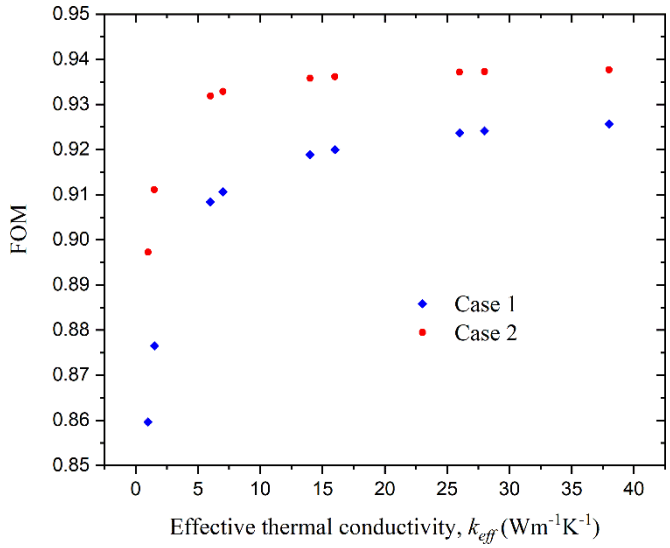

Figure 15: FOM as a function of the effective thermal conductivity k_{eff} for the foam with optimized scattering albedo. The back wall is made of SiC in case 1, while a back wall with an optimized emissivity is considered in case 2. The optimized foam parameters for cases 1 and 2 are respectively provided in Tables 1 and 2.

Table 2: Optimized foam parameters as a function of the effective thermal conductivity k_{eff} for a back wall of SiC (case 1 in Fig. 15).

k_{eff} ($Wm^{-1}K^{-1}$)	β (m^{-1})	L (mm)	ω_1 (-)	ω_2 (-)	$\lambda_{cut\text{-}off}$ (μm)	ε_w (-)	ϕ (-)	FOM
1	1200.0	1.00	2.23E-08	1.0	1.6	SiC	0.950	0.860
1.5	1292.1	1.00	4.47E-08	1.0	1.8	SiC	0.946	0.876
6	1234.6	1.39	1.01E-06	1.0	2.2	SiC	0.949	0.908
7	1223.3	1.46	4.78E-05	1.0	2.2	SiC	0.949	0.911
14	1200.0	1.72	9.32E-08	1.0	2.4	SiC	0.950	0.919
16	1200.0	1.77	2.60E-04	1.0	2.4	SiC	0.950	0.920
26	1200.0	1.97	2.84E-06	1.0	2.5	SiC	0.950	0.924
28	1200.0	1.98	1.59E-08	1.0	2.5	SiC	0.950	0.924
38	1200.0	2.11	1.37E-05	1.0	2.6	SiC	0.950	0.926

Table 3: Optimized foam parameters as a function of the effective thermal conductivity k_{eff} for a back wall with optimized emissivity ε_w (case 2 in Fig. 15).

k_{eff} ($Wm^{-1}K^{-1}$)	β (m^{-1})	L (mm)	ω_1 (-)	ω_2 (-)	$\lambda_{cut\text{-}off}$ (μm)	ε_{w1} (-)	ε_{w2} (-)	$\lambda'_{cut\text{-}off}$ (μm)	ϕ (-)	FOM
1	1200	1.0	1.47E-06	1.0	1.6	1.0	9.60E-08	3.2	0.95	0.897
1.5	1200	1.0	1.11E-08	1.0	1.8	1.0	3.44E-08	3.2	0.95	0.911
6	1200	1.0	6.58E-07	1.0	2.3	1.0	2.53E-06	3.2	0.95	0.932
7	1200	1.0	1.67E-06	1.0	2.3	1.0	9.15E-05	3.2	0.95	0.933
14	1200	1.0	2.52E-07	1.0	2.4	1.0	9.82E-06	3.2	0.95	0.936
16	1200	1.0	3.25E-07	1.0	2.5	1.0	7.28E-07	3.2	0.95	0.936
26	1200	1.0	2.47E-06	1.0	2.5	1.0	2.07E-07	3.2	0.95	0.937
28	1200	1.0	2.82E-06	1.0	2.5	1.0	7.05E-06	3.2	0.95	0.937
38	1200	1.0	1.40E-06	1.0	2.5	1.0	9.15E-06	3.2	0.95	0.938

The FOM can reach a value of ~ 94% by engineering the emissivity of the back wall, the foam scattering albedo, and the foam effective thermal conductivity. For a SiC back wall, the FOM can be enhanced to a value of ~ 90% by solely engineering the foam scattering albedo, and to a value of ~ 92% when both ω and k_{eff} are engineered. From Tables 2 and 3, it is clear that the optimized foam must have a very small scattering albedo for short wavelengths (~ 0) and a very large scattering albedo for long wavelengths (~ 1). This physically makes sense. In the ideal case, short-wavelength solar radiation penetrating the foam is absorbed (small scattering albedo), while long-wavelength radiation emitted by the foam is trapped due to high scattering (large scattering albedo).

Sub-task 1.3: Experimental characterization of VATI foam with concentrated solar simulator and direct measurement of receiver FOM

Milestone 1.3.1 status: 1” diameter SiC foam samples with optimal porosity and thickness (from modeling) were fabricated.

This task was unable to be completed at the end of the performance period. Several technical challenges associated with FOM measurement technique benchmarking (Pyromark 2500 incompatibility with tungsten) prevented testing of SiC VATI samples.

The performance team will continue testing of SiC after benchmarking the measurement technique outside the scope of the current award.

The VATI receiver layer can be characterized in terms of the figure of merit (FOM) that is commonly used to describe solar receiver coatings. This comparison is meaningful because both solar receiver coatings and the VATI layer serve the same purpose (solar-thermal conversion) in a CSP power cycle. Modifications to the conventionally defined FOM is described in context of Subtask 2.2. Specifically, the optical property based FOM can be defined in terms of the thermal fluxes (incident, loss, and converted heat fluxes). Design of the experimental apparatus and uncertainty analysis of reported FOMs are also discussed.

Task 2: Design and fabricate a test chamber to characterize the FOM at high temperatures

Summary: A customized test platform was developed to measure the FOM at 750°C. A reference bar-based technique was developed to directly measure the converted solar-thermal heat rate. Experimental uncertainty analysis was performed to enable <4% error in FOM measurements at 750°C.

Sub-task 2.1: Thermo-fluidic modeling of the cooling heat exchanger for the high-temperature heat flux sensor

Milestone 2.1.1 status: Completed 100% as of 10/1/2019. A reference bar was designed and fabricated that enables FOM measurement across a circular cross-sectional area (1" diameter) at 750°C and a concentration factor of 1000x.

A. Figure of merit

Concentrated solar power (CSP) is a technology that converts solar radiation into thermal energy, which is then used to drive turbines and generate electricity [15], [16]. The efficiency of CSP plants strongly depends on the solar-to-thermal conversion efficiency, also called figure of merit (FOM), of the solar receiver coating (hereafter referred to as receiver). The FOM is defined as the amount of solar radiation absorbed and retained by the receiver divided by the total solar radiation incident on the receiver [17]–[19].Therefore, an ideal receiver should maximize the amount of solar absorption while minimizing thermal emission from the receiver. This can be achieved by spectrally selective surfaces that have large absorptivity within the short-wavelength solar spectrum and low emissivity within long-wavelength receiver emission spectrum [19]. However, for receiver temperatures larger than 500 K, which are typical in CSP plants, perfect spectral selectivity cannot be achieved because of the overlap between the solar and thermal emission spectra. This spectral overlap should be taken into account for the maximum FOM of a solar receiver. The simplest case of an ideal solar receiver can be realized by determining a cut-off wavelength at which the receiver absorptivity transitions from unity to zero[20].

The FOM has been widely used to evaluate the performance of CSP receiver coatings[18], [21]–[24]. However, direct comparison of FOMs calculated under disparate conditions of solar concentrations and temperatures results in misleading interpretation of CSP receiver performances. For example, Ambrosini et al. [18] measured the FOM of a solar receiver made of Pyromark 2500 to be 0.897 at a concentration factor $C = 667$ and a receiver temperature $T_{\mathrm{r}} = 973$ K, while Kim et al. [23] reported a FOM of 0.903 for a copper-alloyed spinel black oxide receiver at $C = 1000$ and $T_r = 1023$ K (here, a

concentration factor is defined as the scalar multiple of the solar flux on earth's surface). However, since they were measured in different operating conditions, it is not possible to objectively claim that one receiver has a better performance than the other simply by comparing the FOM values. The objective of this work is therefore to revisit the interpretation of the FOM and to provide a novel metric, the receiver effectiveness, enabling a direct comparison of CSP receivers working under different concentration factors and temperatures. This is done by defining the *receiver effectiveness* as the ratio of the actual receiver FOM to the maximum FOM for the same concentration factor and temperature. In addition, the maximum CSP plant efficiency is introduced by combining the maximum FOM and the Carnot efficiency to show that the optimal concentration factor and receiver temperature should be selected not based on the FOM but based on the CSP plant efficiency.

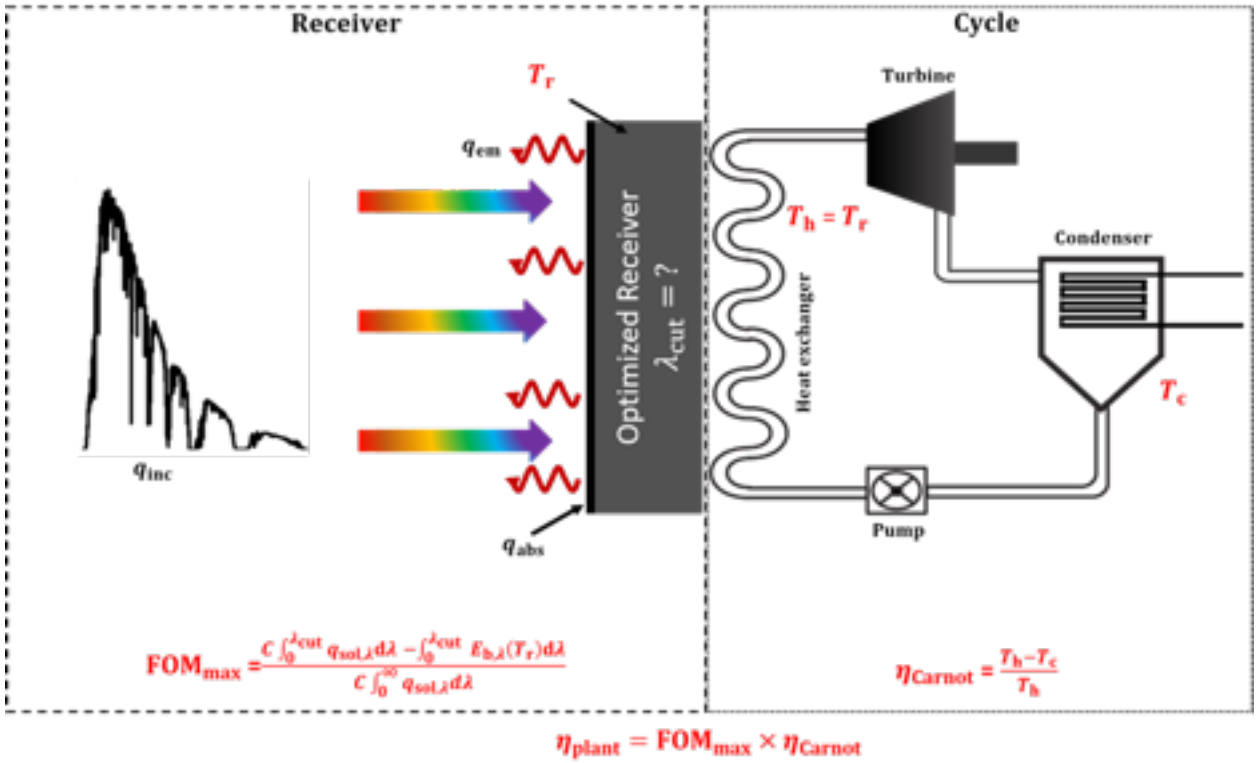

Figure 16: Schematic of an optimized solar receiver and corresponding power cycle. The optimized receiver absorbs and radiates energy up to a certain cut-off wavelength based on its temperature and concentration factor. The resultant net energy is then supplied to the cycle, which generates electricity with an efficiency of Carnot cycle.

Figure 16 illustrates a CSP receiver illuminated by concentrated solar radiation. When concentrated solar radiation is incident onto the receiver, it is either absorbed or reflected. In addition, the receiver emits thermal radiation to the surroundings. The difference between the absorbed solar radiative flux q_{abs} and the emitted radiative flux q_{em} at the receiver temperature T_{r} is the net energy that can be transferred to a heat engine, represented by a thermodynamic cycle, upon absorption. The FOM is defined as this net solar thermal energy normalized by the incident solar radiative flux q_{inc} [17], [18], [25].

$$FOM = \frac{q_{abs} - q_{em}}{q_{inc}} \tag{19}$$

The incident solar radiative flux is calculated as $q_{\mathrm{inc}} = C\int_0^\infty q_{\mathrm{sol},\lambda} d\lambda$, where λ is the wavelength, C is the concentration factor, and $q_{\mathrm{sol},\lambda}$ is the AM 1.5 standard spectral solar flux ("ASTM G173-03 Table", n.d.). The absorbed and emitted radiative fluxes are computed as follows:

$$q_{abs} = C\int_0^\infty \alpha_\lambda q_{sol,\lambda} d\lambda \tag{20}$$

$$q_{em} = \int_0^\infty \varepsilon_\lambda E_{b,\lambda}\left(T_r\right) d\lambda \tag{21}$$

where α_λ and ϵ_λ are respectively the spectral, hemispherical absorptivity and emissivity of the receiver. Here, it is assumed that the receiver is diffuse, such that the spectral, hemispherical absorptivity equals the spectral, hemispherical emissivity according to Kirchhoff's law (i.e., $\alpha_\lambda = \epsilon_\lambda$)[14]. For simplicity, the adjective hemispherical will be omitted in the rest of the text. In Eq. (3), $E_{\mathrm{b},\lambda}(T_{\mathrm{r}})$ is the spectral blackbody emissive power at the receiver temperature. It should be noted that convective heat losses to the surrounding air are not considered in the FOM.

Owing to the overlap between the solar and emission spectra for receiver temperatures larger than 500 K, it is impossible to completely separate the absorption and emission spectra. Therefore, the maximum FOM ($\mathrm{FOM}_{\max}$) is calculated by defining a cut-off wavelength λ_{cut} beyond which further absorption of solar radiation is outweighed by emission losses. The spectral absorptivity of an ideal receiver having the maximum FOM is thus given by:

$$\alpha_\lambda = \acute{\mathrm{U}}_\lambda = \begin{cases} 1 & \lambda \le \lambda_{cut} \\ 0 & \lambda > \lambda_{cut}, \end{cases} \tag{22}$$

which yields the maximum FOM as

$$FOM_{\max} = \frac{C\int_0^{\lambda_{cut}} q_{sol,\lambda} d\lambda - \int_0^{\lambda_{cut}} E_{b,\lambda}\left(T_r\right) d\lambda}{C\int_0^\infty q_{sol,\lambda} d\lambda} \tag{23}$$

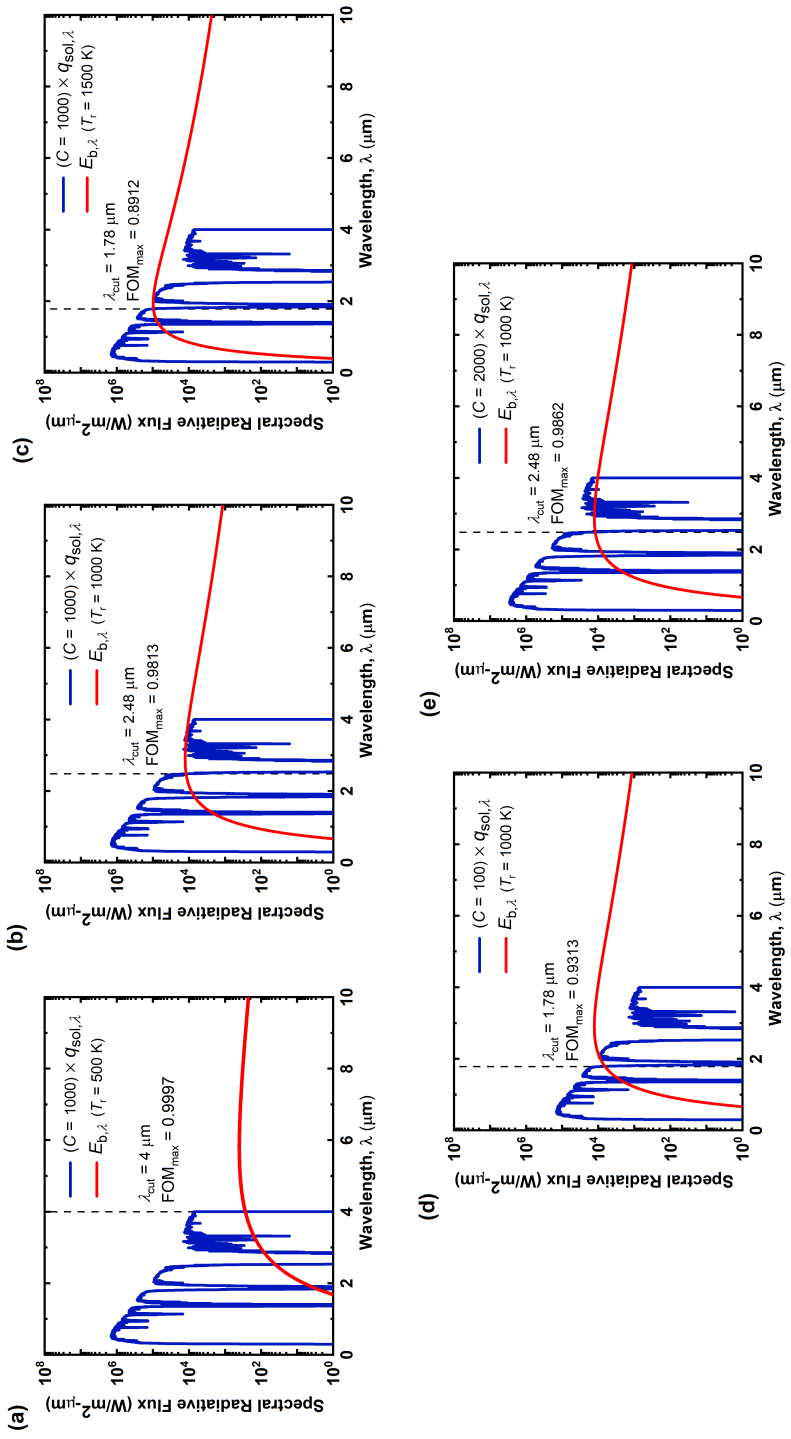

Figure 17: Cut-off wavelength and corresponding maximum FOM (FOM $_{\max}$) for: (a) $C = 1000, T_r$=500 K, (b) $C = 1000, T_r$=1000 K, (c) $C = 1000, T_r$=1500 K, (d) $C = 100, T_r$=1000 K, and (e) $C = 2000, T_r$=1000 K. The cut-off wavelength was selected to maximize the FOM.

Figure 17 shows the cut-off wavelength and the corresponding maximum FOM for five different combinations of concentration factors and receiver temperatures. In panels (a), (b), and (c), the concentration factor is fixed at 1000 while the receiver temperature increases from 500 K to 1500 K. As the receiver temperature increases, the emitted flux increases along with its spectrum shifting towards shorter wavelengths. The latter effect leads to a shift of the cut-off wavelength from 4 μm at T_{r} = 500 K to 1.78 μm at T_{r} = 1500 K owing to a larger overlap between the emission and solar spectra. A shorter cut-off wavelength reduces the solar flux absorbed by the receiver. As a result, a solar receiver at higher temperatures yields a lower FOM due to the diminution of solar absorption as well as the augmentation of thermal emission.

In panels (d), (b), and (e) of Fig. 2, the receiver temperature is fixed at 1000 K while the concentration factor increases from 100 to 2000. Varying the concentration factor does not affect the spectral distribution of solar radiation, whereas the same receiver temperature maintains the thermal emission spectrum as well. Yet, the cut-off wavelength is impacted by the concentration factor because of the competition between the absorbed solar flux and the emitted flux. Here, the cut-off wavelength increases from 1.78 μm to 2.48 μm for a rise in concentration factor from 100 to 1000. Although the emitted flux increases due to the longer cut-off wavelength, the ten-fold enhancement in the magnitude of the incident solar flux mitigates the negative impact of the emitted flux to yield a higher FOM at $C = 1000$. When the concentration factor increases from 1000 to 2000, the enhancement of the FOM is modest, and the cut-off wavelength remains the same. This is explained by the fact that the solar spectrum has a negligible amount of energy contained at wavelengths longer than 2.48 μm. Clearly, the receiver temperature has a more significant impact on the cut-off wavelength than the concentration factor.

Figure 3(a) shows the maximum FOM as a function of the concentration factor and receiver temperature. A higher concentration factor and lower receiver temperature mitigate the impact of emission losses and therefore lead to a larger maximum FOM. Figure 3(b) shows FOM values from various contemporary literature sources, measured at different concentration factors and receiver temperatures, against the maximum FOM curves. Clearly, direct comparison of FOMs measured with different concentration factors and receiver temperatures is inappropriate and misleading. It is thus more meaningful to correlate the FOM to their respective maximum values, akin to the second law efficiency in thermodynamics. For this purpose, a novel metric called the receiver effectiveness is proposed and is defined as:

$$e = \frac{FOM_{act}}{FOM_{max}} \tag{24}$$

where $\mathrm{FOM}_{\mathrm{act}}$ and $\mathrm{FOM}_{\mathrm{max}}$ are respectively the actual and maximum FOM values. Table 1 compares the effectiveness values from the FOMs reported in the literature and their corresponding operating conditions. Although in general a solar receiver having a high FOM yields a high effectiveness, Table 1 clearly demonstrates that a higher FOM does not necessarily lead to a higher effectiveness unless measured at the same operating conditions. For example, FOMs of 0.895 and 0.882 have been reported by Avila-Marin et al.[21] and Moon et al.[22], respectively. Direct comparison of these FOMs would lead to the conclusion that Ref.[21] reported a better performing receiver than Ref.[22]. However,

the effectiveness of the receiver in Ref. [22] is 0.9, which is slightly higher than the receiver effectiveness of 0.897 in Ref. [21]. Therefore, contrary to considering solely the FOM, this effectiveness formulation provides a different perspective for determining the performance of a receiver and is useful for comparing receiver performances independently of their operating conditions.

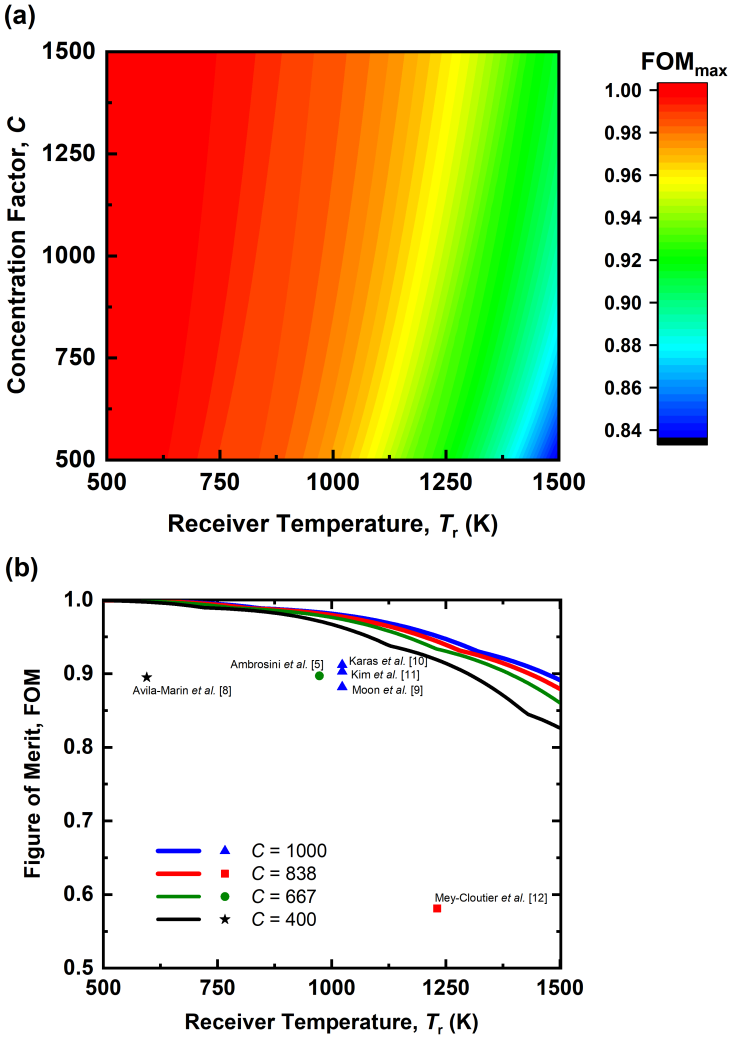

Figure 18: Optimized FOM (FOM_{max}) as a function of receiver temperature and concentration factor in the form of: (a) Contour plot, and (b) Line plot with literature data. The literature data consists of FOM values from Avila-Marin et al. [21], Moon et al. [22], Ambrosini et al. [18],Karaset al. [23],Kim et al. [26], and Mey-Cloutier et al.[24]

The thermal energy retained by the receiver is supplied to a heat engine (or cycle) for power generation (see Fig. 1). As such, the selection of the concentration factor and receiver temperature for optimal CSP plant operating conditions should not be solely based on the FOM. According to the Carnot efficiency, it is desirable to have a high hot-side temperature in order to maximize the cycle efficiency. However, a high temperature on the hot side of the cycle implies a high receiver temperature, which result in large emission losses. There should be an optimal balance between the cycle efficiency and the receiver FOM that results in the highest performances. The interplay between these

two factors is quantified via the theoretically maximum CSP plant efficiency (i.e., solar-to-electrical conversion efficiency) calculated as follows:

$$\eta_{plant} = FOM_{max} \times \eta_{Carnot} \tag{25}$$

where $\eta_{\mathrm{Carnot}} = (T_{\mathrm{r}} - T_{\mathrm{c}})/T_{\mathrm{r}}$ is the Carnot efficiency. Here, it is assumed that the hot reservoir temperature of the Carnot heat engine is equal to the receiver temperature (T_{r}), while the cold-side temperature (T_{c}) of the cycle is equal to the surrounding temperature of 298 K. It should be noted that the maximum FOM can be considered as the theoretical limit of the receiver efficiency with no other optical, thermal and parasitic losses.

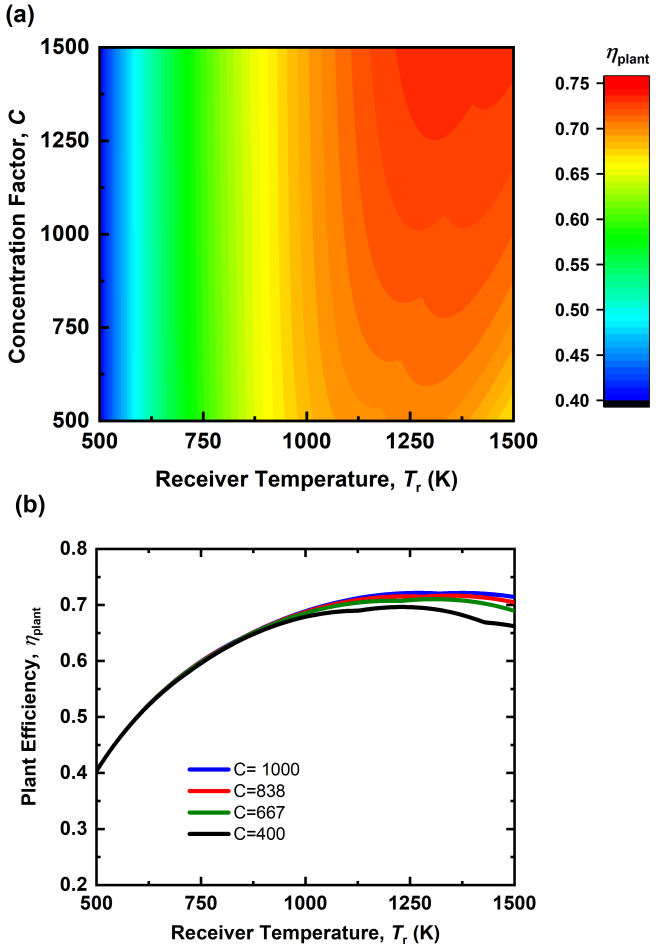

Figure 19: Optimized plant efficiency in the form of: (a) Contour plot, and (b) Line plot as a function of receiver temperature and concentration factor.

The maximum CSP plant efficiency is displayed as a contour plot in Fig. 4(a), and line curve in Fig. 4(b) as a function of the receiver temperature for different concentration factors. This is the theoretical limit of plant efficiency for a given set of operating conditions. Clearly, the plant efficiency cannot be maximized by arbitrarily selecting the concentration factor and receiver temperature. Figure 4(b) shows that there is an optimum receiver temperature maximizing the plant efficiency for a specific concentration factor. Moreover, it is evident that considering solely the FOM does not give a complete picture

of CSP plant performance. If a low receiver temperature is maintained to enhance the FOM, the absorbed energy may not be usable for power generation that demands a high-temperature heat source. Conversely, if the receiver temperature exceeds the optimal point in an attempt to improve the cycle efficiency, a large thermal emission loss from the receiver ultimately degrades the CSP plant performance.

Although the FOM is a widely accepted metric to evaluate the performance of a CSP receiver, direct comparison between FOM values without careful consideration of operating conditions may lead to inaccurate assessment for CSP performance. In the present article, a novel metric called the CSP receiver effectiveness was defined as the ratio of the actual receiver FOM and its maximum value. The effectiveness enables direct comparison of CSP receiver performances under disparate operating conditions. In addition, the CSP plant efficiency was defined by combining the FOM and the Carnot efficiency. It was shown that the optimal combination of concentration factor and receiver temperature should be determined using the maximum CSP plant efficiency. The analysis presented in this paper provides guidelines for designing CSP receivers maximizing the overall solar-to-electrical conversion efficiency.

B. Figure of merit – thermal definition

The FOM is defined as follows, where α is the solar absorptivity, $\cup$ is the emissivity, σ is the Stefan-Boltzman constant, T_s is the surface temperature of the absorber, and q''_{solar} is the total incident solar heat flux:

$$\mathrm{FOM} = \frac{\alpha C q''_{sol} - \varepsilon \sigma T^4}{C q''_{sol}} \tag{26}$$

Based on an energy balance around the receiver coating:

$$q''_{solar} = q''_{emit} + q''_{conv} + q''_{reflected} + q''_{converted} \tag{27}$$

Neglecting the convective losses in a vacuum experiment, Eq. (27) is rewritten as:

$$q''_{converted} = q''_{solar} - q''_{emit} - q''_{reflected} \tag{28}$$

Recognizing that Eq. (28) is the numerator in Eq. (26), the FOM can be expressed as:

$$\mathrm{FOM} = \frac{q''_{converted}}{q''_{solar}} \tag{29}$$

The transformation described above enables the thermal measurement of FOM of receiver coatings. The numerator of Eq. (29) is measured using a tungsten reference bar. The bar maintains a uniform temperature in the radial direction, and this technique has been adopted widely to characterize the thermal conductivity of materials and measure heat flux in phase change (boiling/condensation) experiments. The specific considerations that dictate the design of the reference bar at high temperatures are discussed below and represent an important metrology advancement for CSP receiver development. The incoming solar irradiation. q''_{solar}, is measured independently using a commercial heat flux sensor (Vatell TG-1000). Note that a commercial heat flux sensor cannot be directly used as they are not rated for high temperature (750°C) operation.

C. Reference bar design

Tungsten was chosen as the bar material due to its stability at high temperatures and relatively high thermal conductivity of 197 W/m-K at room temperature[27]. High thermal conductivity is important because materials with high thermal conductivity approximate one-dimensional heat flow better than materials with low thermal conductivity. Assuming one-dimensional heat flow, Fourier's law provides the heat flux as:

$$q'' = -k\frac{dT}{dx} \tag{30}$$

where $q''$is the heat flux, k is the thermal conductivity, T is temperature, and x is the position on the bar. If the temperature distribution is linear, Eq. (30) can be written as:

$$q'' = k\frac{T_1 - T_2}{\Delta x} \tag{31}$$

where T_1, T_2, and Δx are measured experimentally using resistance temperature detectors (RTDs) and micrometers and k is determined from the literature. The first and second subscripts refer to the measurements at any two different locations on the bar. To collect data that better simulate operating conditions, it is desirable that one side of the tungsten bar be maintained at the operating temperature of the solar collector ($\sim$750°C), but in order to maintain equilibrium in the bar, the other end must be cooled. A finite-difference model is developed to determine if the temperature distribution is linear. The temperature at each node was calculated by assuming an average thermal conductivity between two nodes, no heat loss or lateral heat flow, and an input heat flux at the first node. Grid independence was achieved with ~100 nodes for a 10 cm long bar. The temperature change throughout the tungsten bar was predicted to be linear, with a linear regression coefficient of 0.9984. With this calculation's results as a baseline, a 3D finite element calculation was developed in COMSOL Multiphysics to incorporate multi-dimensional conduction, convection in the cooled section, and radiative heat loss. This model was also utilized to determine the cooling load requirements at the cooling side of the bar. The model setup and boundary conditions are shown in Fig. 20.

Parametric calculations were used to determine the bar geometry and cooling flux that would satisfy the temperature and input heat flux conditions. Since the top surface needs to achieve a temperature of 750°C, the length of the bar had to be increased to reach this temperature. The reference bar diameter was specified as 2.54 cm. This diameter was chosen because bar stock of this size is common. The base of the reference bar was designed to mate with a rectangular block with 3x surface area to achieve heat spreading. By changing the length of the bar and observing its effects on temperature, the ideal configuration was determined to be a height of 10 cm, a diameter of 2.54 cm at the heating side, and a diameter of 7.62 cm at the cooling loop side for the given boundary conditions. Radiative heat loss was modeled using an emissivity of 0.04 for polished tungsten.

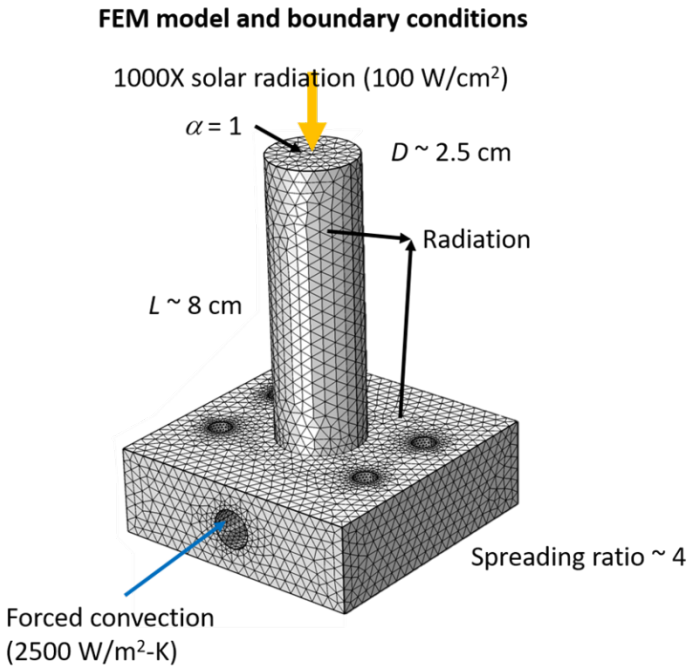

Figure 20: Model setup and boundary conditions used to design the high-temperature reference bar.

It is important to note that the reference bar technique is restricted in its accuracy due to the heat loss that occurs by all exposed surfaces of the bar above the first temperature measurement location. High accuracy Class-A RTD's are restricted to a maximum temperature of 600°C, and thus dictates that a finite heat loss be considered. Reduction in heat loss through the inclusion of high-temperature insulation (k = 0.25 W/mK at 1000K). The insulation layer thickness was determined from the lowest possible thickness available for a range of high-temperature insulation materials. This was found to increase the heat loss due to an increase in emissivity and surface area. An interesting observation is that setting T_1 = 600°C and T_2 = 400°C, results in a larger uncertainty in the FOM than setting T_1 = 500°C and T_2 = 300°C. This is because the uncertainty of the temperature measurements scales with the absolute value of the reading. Temperature measurements at 500 °C and 300 °C resulted in lower heat loss across the measurement volume while also reducing measurement uncertainty. This reduction in uncertainty offsets the increased heat loss from moving lower down the bar. The heat loss of the 500°C to 300°C zone is 11.7% higher than the heat loss of the 600°C to 400°C zone, but the uncertainty reduces by 17.1%. The technique adopted to estimate the propagated uncertainty is described in a subsequent section below. The heat loss term accounts for roughly 1% of the total incoming heat flux for the final design of the reference bar. This linear bias (underprediction) will be accounted for when reporting FOM data for solar selective coatings and VATI foams.

D. RTD calibration

As we are using 2-wire RTDs for the reference bar temperature measurement, calibration with more accurate 4-wire RTD is necessary to eliminate the error due to the lead wire resistance. A 4-wire platinum resistance thermometer from Fluke calibration (model:

5609) was used for the calibration, which has an accuracy of 0.01 K. A field metrology well (Fluke 9144) was used to keep all the RTDs at a constant temperature with minimal fluctuation. The calibration was performed for a temperature range of 25-625°C. It should be noted that the uncertainty in the resistance measurement by the data acquisition setup will also propagate to the temperature measurement. We have used a RTD analog input module by National Instrument (NI 9216) to measure the resistance. The uncertainty in the resistance measurement (U_R) can be considered as $U_R = Gain \times R + Offset$, where R is the measured resistance. The value of *Gain* and *Offset* was found respectively as 0.048% and ±0.101Ω from the product dataset. Individual uncertainties were propagated to calculate the uncertainty of the temperature measurement. As an example of the calibration, the measured resistance and the resultant temperature, along with their uncertainties for our RTD 2 is shown in table 4.

It should be noted that the data from Table 4, shows a linear trend, as shown in Fig. 21. Here, the value of uncertainty is negligible compared to the original value that the error bars are not visible in the figure.

Table 4: Measured resistance and corresponding temperature after calibration of RTD2

Measured resistance (Ohms)	Calculated temperature (°C)
110±0.1538	24.37±0.62
133.3±0.1650	84.48±0.533
156.7±0.1762	146.10±0.55
180±0.1874	209.1±0.61
203.3±0.1986	273.60±.67
226.7±0.2098	339.50±0.70
250±0.2210	406.90±0.73
273.3±0.2322	475.70±0.79
296.7±0.2434	546.00±0.90
320±0.2546	617.70±1.10

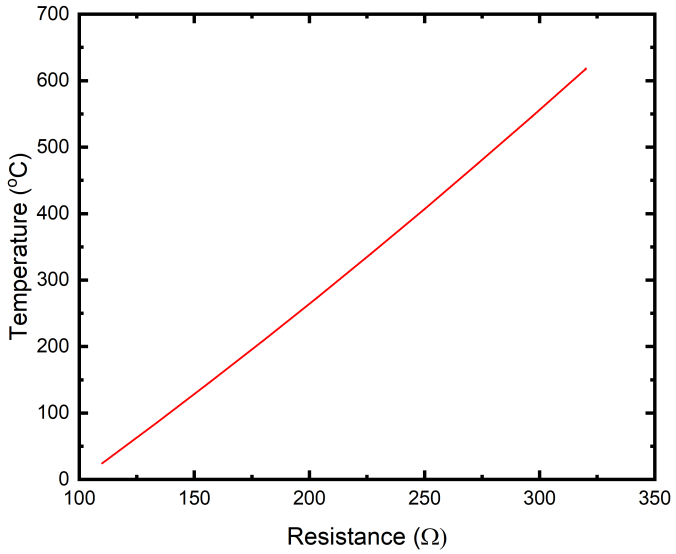

Figure 21: Temperature as a function of measured resistance as calibrated for RTD 2. The errors bars are plotted but not visible due to the high measurement accuracy (see Table 4 for values).

E. Experimental procedure

A solar simulator (SciTech) supplies a concentration of 1000 times the irradiation of the sun on the Earth's surface. The simulator is a high-powered focused beam arc lamp with a capacity of up to 6.5 kW. The focal point of the solar simulator was adjusted to be a circle with the same diameter as the reference bar, which ensures that a uniform heat flux profile is incident on the bar. Two Thorlabs PT1-Z8 stages with Z825B motor actuators were used as a mobile base for the reference bar. The stages are placed on top of each other to control movement in the X and Y directions. The stages have a locational accuracy of ±1.0 m.

First, the heat flux meter (Vatell TG-1000) is placed on the stage inside the vacuum chamber. Next, the solar simulator is turned on, and the heat flux is measured by the heat flux meter (HFM) to give us a baseline measurement. Once this measurement is taken, the HFM is replaced by the reference bar, which is placed in the same location as the HFM, and the lamp is turned on. Once a steady-state is achieved, the temperature measurements from the RTDs are used in conjunction with the thermal conductivity data to determine the heat flux through the reference bar. If the difference in reference bar and HFM measurements is small, then it can be reasonably assumed that the reference bar is working as intended.

As seen in previous sections, heat loss reduction increases the accuracy of heat flux measurements. Therefore, to mitigate the effect of natural convection on the reference bar, experiments were performed in a vacuum. The vacuum chamber included a drilled hole pattern in the floor, which aided in the precise relocation of the stages and reduced variation between experiments. The vacuum chamber's walls include welded flow channels for the coolant from an ATC K6 6.0 kW capacity chiller. Ports in the vacuum chamber allow for the transfer of cooling fluid into the reference bar base, electrical signals to control the stages, data transfer from the RTDs, and data transfer from the pressure transducer. The chiller that supplies the cooling fluid for the reference bar is an

ATC K1 1.75 kW capacity chiller. An MKS vacuum pressure transducer is used to estimate the vacuum condition in the chamber. Both the vacuum chamber and solar simulator sit on an optical table to ensure that the beam from the solar simulator is perpendicular to the top surface of the reference bar

F. Uncertainty analysis

An uncertainty analysis was performed on the multivariate measurement of FOM that measured the effect of temperature sensor error, location measurement error, heat loss, and thermal conductivity error. The absolute uncertainty in temperature and location measurements is a consequence of the errors associated with sensors and measurement devices (Table 5). A perfect absorber and zero emittance was additionally assumed.

The total uncertainty in the measured FOM is ±4%. Further refinements are possible with high accuracy thermal conductivity measurements and use of a laser power meter to measure the incoming solar irradiation.

Table 5: Variables used to calculate the FOM and their associated uncertainties. Note that for the purpose of illustrated, nominal values for T_1 = 500°C and T_2 = 300°C are assumed.

Measured parameter	Nominal measurement	Uncertainty	Percentage of total uncertainty
x_1 (cm)	6.70	$\pm 2.54 \times 10^{-3}$	0.05
x_2 (cm)	4.00	$\pm 2.54 \times 10^{-3}$	0.05
T_1 (°C)	500	±1.15	1.79
T_2 (°C)	300	±0.75	0.76
Solar simulator irradiance (W/cm^2)	100	±3.00	48.69
Tungsten thermal conductivity at 500°C (W/m-K)	132.60	±3.978	48.67
FOM	0.99	0.04	-

Milestone 2.1.2 status: Incomplete at the end of the award period. Pyromark 2500 coating on tungsten was discovered to be unstable upon exposure to concentrated solar irradiation. Oxidized Inconel 625 was identified as a suitable alternative.

Many issues were discovered with the use of Pyromark as a solar absorber (see Fig. 22) 1) Pyromark does not bond well with tungsten and requires precise surface conditions and film thickness to cure. 2) Pyromark appears to be unstable during high-temperature operation, even under vacuum conditions, also when not using tungsten as the substrate; the Pyromark turns a reddish-brown color in response to temperatures exceeding 750°C. 3) Thicker Pyromark layers tend to cause delamination and an unstable cure. Shown in Fig. 16 are three samples of Pyromark cured on different substrates. The first sample is untreated, the second sample is Pyromark on nickel after being exposed to 1000x irradiation for 20 minutes, and the last sample is Pyromark on tungsten after being

exposed to 1000x irradiation for 1 hour. The same reddish-brown color appears in the treated samples: a small strip on the nickel sample and the entire surface on the tungsten sample. These results lead to the conclusion that Pyromark is unstable at these operating conditions.

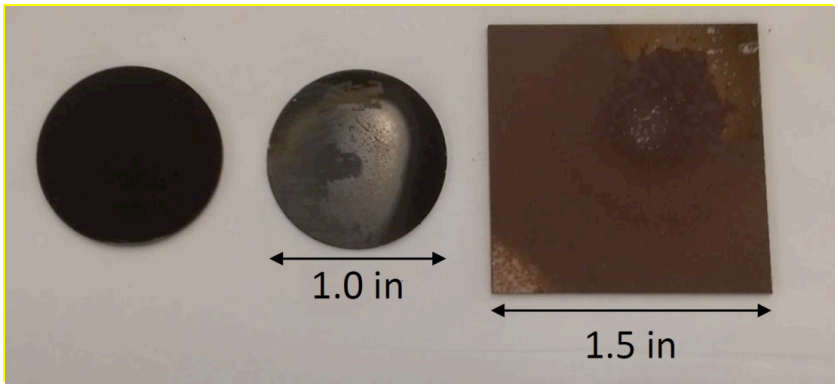

Figure 22: Pyromark 2500 instability. From L to R. a) Pyromark on Nickel (cured, unexposed), b) same sample as a) but after 20 minutes exposure to 1000X irradiation, c) Pyromark on tungsten sheet

Oxidized Inconel-625 was evaluated as an alternative to Pyromark 2500. Oxidized Inconel-625 has favorable absorptive properties to enable broad-band solar thermal conversion [16]. Room temperature optical properties for Inconel-625 and other oxides have been reported by Colas and co-workers[28].

1” diameter Inconel-625 sheets were cut from a sheet using wire electrical discharge machining. The surface of the disc was grit blasted (200 mesh size). Next, the discs were cleaned using iso-propyl alcohol and acetone to remove contaminants. A native oxide on the surface was generated by heating the sample in a high-temperature furnace at 1000°C for 12 hours. One side of the disc was cleaned and polished for bonding to the reference bar assembly (example bond is shown in Fig. 23). A high-temperature thermally conductive bonding technique was developed using a vacuum brazing process. A high-purity active braze alloy of gold (96.4%), nickel (3%), and titanium (0.6%) was ultimately selected after multiple trials. Solidus and liquidus temperatures of 1030°C and 1003°C enable testing at 750°C. Additionally, the braze foil has an estimated thermal conductivity of 25 W/m-K, enabling lower thermal contact resistance and higher accuracy of FOM measurements.

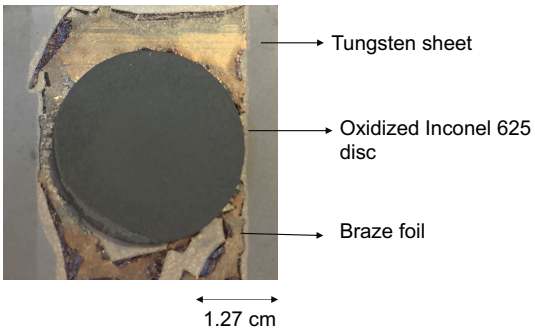

Figure 23: Successful tungsten-oxidized Inconel 625 bond.

Sub-task 2.2: Design and fabricate custom temperature-controlled vacuum chamber for FOM measurement.

Milestone 2.2.1 status: Completed 100% as of 8/1/2020. Vacuum level <10 mTorr and wall temperature increase during solar simulator operation < 2°C.

A. Vacuum chamber design and construction

The primary function of the vacuum chamber is to enable FOM measurements. In addition, the chamber must allow: a) Optical access to incoming irradiation from the solar simulator, b) Coolant flow to cool reference bar base, c) Signal outflow, d) and isothermal walls. The overall configuration of the test setup is summarized in Fig. 24.

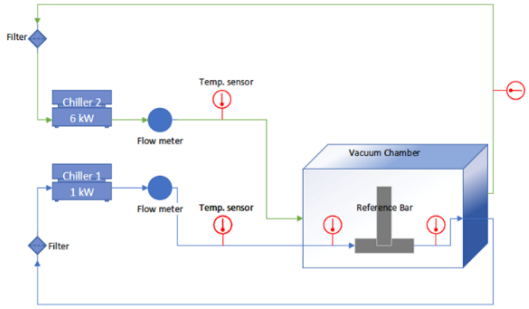

Figure 24: Design of the coolant loop to a) extract heat from the bottom of the reference bar and b) maintain isothermal walls of the vacuum chamber for accurate determination of radiative heat losses.

X-Y translational ability to move the sample and correct for minor changes in beam alignment without having to open the chamber is an important consideration. An adapter and a pair of piezo-electric stages was designed and integrated (Fig. 25).

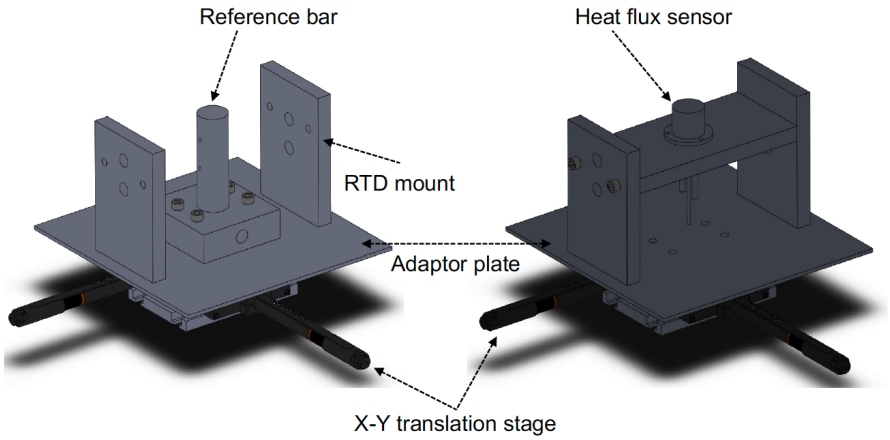

Figure 25: Overview of the stages developed to measure the converted and the incoming solar heat flux with the reference bar and the commercial heat flux sensor.

Fig. 26 shows the finalized experimental setup. Using a water-cooled heat flux sensor, incoming solar irradiation of 100 W/cm^2 (or 1000x concentration) was measured successfully with an uncertainty of ±2%. The sensor temperature was recorded as 278K.

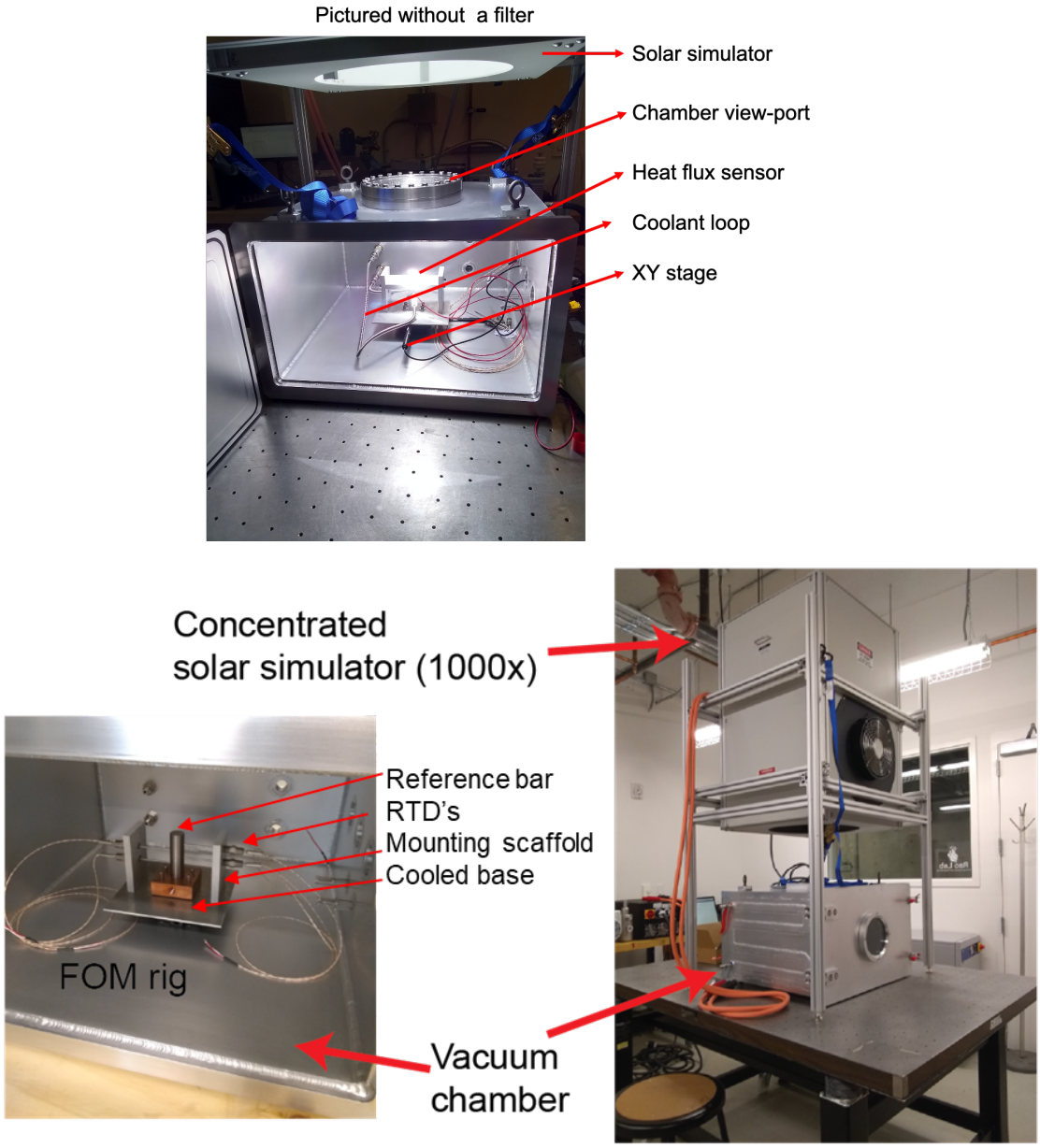

Figure 26: Finalized high-temperature FOM measurement setup

Task 3: Development of concentrated solar simulator

Summary: A concentrated solar simulator was designed, fabricated, and tested. Output: 880 to 1700X concentration factor across a 1" diameter circular cross-sectional area.

Sub-task 3.1: Design and develop elliptical reflector geometry and select high power lamp

Milestone 3.1.1 status: Completed 100% as of 10/1/2019. A 6.3 kW lamp and reflector were selected.

Sub-task 3.2: Construction of a concentrated solar simulator to enable VATI foam testing

Milestone 3.2.1 status: Completed 100% as of 2/7/2020. The solar simulator performance was experimentally characterized to demonstrate concentration factors of 800-1700X over a 1" diameter cross sectional area.

The concentrated solar simulator was co-designed based on the reference bar and chamber design. This is due to the strong dependence of the irradiation intensity of the z-plane (vertical) position. The focal plane was determined to be 497 mm (defined with respect to the parabolic reflector), coinciding with the top of the reference bar/VATI foam sample. The produced solar irradiation was quantified both in terms of averaged intensity as well as the expected intensity distribution (mostly Gaussian). The incident solar intensity was quantified with a calibrated (1% error) laser power meter (FLASH-3K-55-C). In addition, to probe the irradiation intensity, we designed 3 different sized apertures – 25.4, 19-, and 12.7-mm diameter. The hypothesis here is that if the beam profile is sufficiently uniform/homogenous, as the aperture diameter is decreased, the measured intensity must scale linearly with decreasing area. The measurement results are summarized in Fig. 27:

	Value	Units	Notes
Power Measurement, 25.4 mm Aperture	848	W	Power Supply Setting: 100% 170.0 W/cm^2, 1700 Suns
Power Measurement, 25.4 mm Aperture	501	W	Power Supply Setting: 68% 100.5 W/cm^2, 1005 Suns
Power Measurement, 25.4 mm Aperture	495	W	Power Supply Setting: 67% 99.3 W/cm^2, 993 Suns
Power Measurement, 19.05 mm Aperture	381	W	Power Supply Setting: 67% 133.7 W/cm^2, 1337 Suns
Power Measurement, 12.7 mm Aperture	267	W	Power Supply Setting: 67% 210.8 W/cm^2, 2108 Suns
Ambient Temperature During Classification:	22	Celsius	
Measurement Date:	21 January 2020		

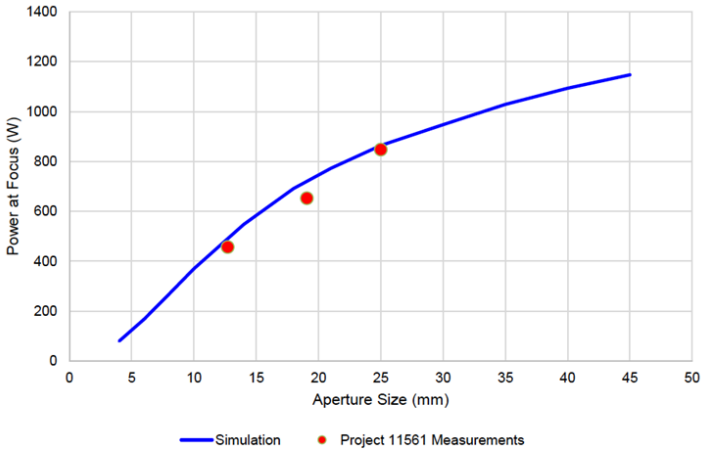

Figure 27: Results from the calibration of the concentrated solar simulator, highlighting the completion of Milestone 3.1.1 and 3.2.1

The beam profile of the solar simulator was found by adjusting the X-Y position of the heat flux sensor using the motor actuated stages. The solar simulator was set at its lowest power level (63% of the maximum) to perform this measurement. Firstly, we found the position of the stages where the heat flux reading is maximum, which was at X = 13 mm and Y=11.5 mm with a heat flux of 108 W/cm^2 (~1080 suns) for our current experimental setup. Then we fixed the Y stage at 13 mm and moved the X stage for its entire travel range (0 to 25 mm) with an interval of 1 mm. Similarly, the Y stage was moved from 0 to 25 mm while keeping the X stage at 13 mm. The resultant heat flux reading changed between 46.5 to 108 W/cm^2 for the X stage movement while it was between 47 to 108 W/cm^2 for the Y stage movement. This beam profile can be further used as the location-based incident solar heat flux $\left(q''_{solar}\right)$ in the measurement of FOM.

Significant Accomplishments and Conclusions

Converting concentrated solar irradiation to heat using volumetric absorption and subsequent transfer to the working fluid boundary is a novel approach that has not been well explored in the CSP community. Note that volumetric absorption in flow through receivers, though similar has markedly different constraints. For instance, in a flow through receiver it is important to achieve a balance between heat transfer and pressure drop. In contrast, for the VATI receiver, it is important to maximize absorption and to reduce the conduction resistance and low-pressure drop is not a requirement. A comprehensive modeling framework was developed as part of this work that accounts for the random geometry of open-cellular frameworks. Realistic 3D geometries obtained from micro X-ray CT scans were integrated with a MCRT framework. Thus, a procedure was developed to account for the structure of the open-cellular porous networks and calculate structure-dependent properties such as, extinction coefficient, scattering albedo and phase function. The radiative transfer equation and Fourier's law were used to model the thermalization of incoming solar irradiation, scattering, emission, and conduction. With commercially available SiC foams, a FOM of 0.84 was predicted. Further optimization of the foam structure and properties led to a theoretical FOM of 0.92.

The figure of merit, a commonly used metric to compare solar selective coatings, is typically estimated from room temperature optical property measurements. A high-accuracy technique to measure FOM at CSP operational temperatures (1000 K) was developed in this effort. A 1-D heat conduction-based technique was developed, which predicts the FOM in a vacuum, based on converted heat flux measurements. On-sun, high-temperature receiver performance data is inherently valuable to the CSP community. The uncertainty in reported FOM was predicted based on a rigorous uncertainty propagation analysis. It is anticipated that the characterization of common selective coatings and the VATI foam will be characterized and published in prominent solar energy journals. At the onset of the project, Pyromark 2500 was chosen as a candidate material to benchmark the FOM metrology, however, stable coatings of Pyromark have not been realized. To address this challenge, alternative coatings such as metal oxides and cermets are currently under investigation.

Inventions, Patents, Publications, and Other Results

Conference presentations:

1. R Crist, M Francoeur, K Park, and S R. Rao, "*Development of Metrology for the High-temperature Characterization of Solar-Thermal Receivers*", 13135, IMECE2019, SLC, UT 11/11-11/14 2019.

2. A. N. M. T. Elahi, M. Ghashami, D. Jensen & K. Park, "Comprehensive Energy Balance Analysis of Photon-Enhanced Thermionic Emission for Concentrated Solar Power Generation", 12663, IMECE2019, SLC, UT 11/11-11/14 2019.

Peer-reviewed journal articles:

1. A. N. M. T. Elahi, D. Jensen, M. Ghashami, K. Park. "Comprehensive Energy Balance Analysis of Photon-Enhanced Thermionic Power Generation Considering Concentrated Solar Absorption Distribution," *Solar Energy Materials and Solar Cells*, Vol. 226, p. 111067, 2020.

2. R. Crist, A. N. M. T. Elahi, V. Hatamipour, M. Francoeur, S. R. Rao, K. Park. "Revisiting the Figure of Merit of Concentrated Solar Power Receivers", under review, *ASME Journal of Solar Energy Engineering*, (arXiv preprint arXiv:2012.02841).

Path Forward

FOM characterization efforts will continue after the termination of this project. Well quantified FOM data is limited in contemporary literature. In addition, limited information is also available regarding the uncertainty in these measurements. Researchers often rely on room-temperature optical data to extrapolate the FOM at high temperatures – there is no validation available to ascertain if changes in optical properties across the wavelength spectrum relevant for CSP (UV-VIS-IR) at high temperatures (~1000K). The FOM for VATI foam (SiC) and other candidate materials will also be tested and reported in prominent academic journals relevant to CSP/solar technologies. The performance team is also making advancements on hierarchically porous volumetric receivers.

References:

[1] C. K. Ho, A. R. Mahoney, A. Ambrosini, M. Bencomo, A. Hall, and T. N. Lambert, "Characterization of Pyromark 2500 Paint for High-Temperature Solar Receivers," *J. Sol. Energy Eng.*, vol. 136, no. 1, Jul. 2013.

[2] D. Chester, P. Bermel, J. D. Joannopoulos, M. Soljacic, and I. Celanovic, "Design and global optimization of high-efficiency solar thermal systems with tungsten cermets," *Opt. Express*, vol. 19, no. S3, pp. A245–A257, 2011.

[3] F. Cao *et al.*, "A high-performance spectrally-selective solar absorber based on a yttria-stabilized zirconia cermet with high-temperature stability," *Energy Environ. Sci.*, vol. 8, no. 10, pp. 3040–3048, 2015.

[4] F. Cao, K. McEnaney, G. Chen, and Z. Ren, "A review of cermet-based spectrally selective solar absorbers," *Energy Environ. Sci.*, vol. 7, no. 5, pp. 1615–1627, 2014.

[5] X. Wang, X. Yu, S. Fu, E. Lee, K. Kekalo, and J. Liu, “Design and optimization of nanoparticle-pigmented solar selective absorber coatings for high-temperature concentrating solar thermal systems,” *J. Appl. Phys.*, vol. 123, no. 3, p. 33104, Jan. 2018.

[6] J. Petrasch, P. Wyss, and A. Steinfeld, “Tomography-based Monte Carlo determination of radiative properties of reticulate porous ceramics,” *J. Quant. Spectrosc. Radiat. Transf.*, vol. 105, no. 2, pp. 180–197, Jun. 2007.

[7] M. A. Badri, Y. Favennec, P. Jolivet, and B. Rousseau, “Conductive-radiative heat transfer within SiC-based cellular ceramics at high-temperatures: A discrete-scale finite element analysis,” *Finite Elem. Anal. Des.*, vol. 178, p. 103410, 2020.

[8] R. Coquard, D. Baillis, and J. Randrianalisoa, “Homogeneous phase and multi-phase approaches for modeling radiative transfer in foams,” *Int. J. Therm. Sci.*, vol. 50, no. 9, pp. 1648–1663, 2011.

[9] S. Cunsolo, D. Baillis, and N. Bianco, “Improved Monte Carlo methods for computational modelling of thermal radiation applied to porous cellular materials,” *Int. J. Therm. Sci.*, vol. 137, pp. 161–179, 2019.

[10] M. Bracconi, M. Ambrosetti, M. Maestri, G. Groppi, and E. Tronconi, “A fundamental analysis of the influence of the geometrical properties on the effective thermal conductivity of open-cell foams,” *Chem. Eng. Process. - Process Intensif.*, vol. 129, no. April, pp. 181–189, 2018.

[11] J. I. Larruquert, A. P. Pérez-Marín, S. García-Cortés, L. R. Marcos, J. A. Aznárez, and J. A. Méndez, “Self-consistent optical constants of SiC thin films,” *J. Opt. Soc. Am. A*, vol. 28, no. 11, pp. 2340–2345, Nov. 2011.

[12] S. Wang *et al.*, “4H-SiC: a new nonlinear material for midinfrared lasers,” *Laser \& Photonics Rev.*, vol. 7, no. 5, pp. 831–838, 2013.

[13] T. J. Hendricks and J. R. Howell, “Absorption/scattering coefficients and scattering phase functions in reticulated porous ceramics,” *J. Heat Transfer*, vol. 118, no. 1, pp. 79–87, 1996.

[14] M. F. Modest, *Radiative heat transfer*. Academic press, 2013.

[15] A. B. Meinel, M. P. Meinel, and P. E. Glaser, “Applied Solar Energy: An Introduction,” *Phys. Today*, vol. 30, no. 1, pp. 66–66, Jan. 1977.

[16] P. Bermel, J. Lee, J. D. Joannopoulos, I. Celanovic, and M. Soljacie, “Selective Solar Absorbers,” *Annu. Rev. Heat Transf.*, vol. 15, no. 15, pp. 231–254, 2012.

[17] L. Cindrella, “The real utility ranges of the solar selective coatings,” *Sol. Energy Mater. Sol. Cells*, vol. 91, no. 20, pp. 1898–1901, 2007.

[18] A. Ambrosini, A. Boubault, C. K. Ho, L. Banh, and J. R. Lewis, “Influence of application parameters on stability of Pyromark® 2500 receiver coatings,” *AIP Conf. Proc.*, vol. 2126, no. 1, p. 30002, 2019.

[19] L. A. Weinstein, J. Loomis, B. Bhatia, D. M. Bierman, E. N. Wang, and G. Chen, “Concentrating Solar Power,” *Chem. Rev.*, vol. 115, no. 23, pp. 12797–12838,

Dec. 2015.

[20] K. Burlafinger, A. Vetter, and C. J. Brabec, “Maximizing concentrated solar power (CSP) plant overall efficiencies by using spectral selective absorbers at optimal operation temperatures,” *Sol. Energy*, vol. 120, pp. 428–438, 2015.

[21] A. L. Avila-Marin, M. Alvarez de Lara, and J. Fernandez-Reche, “Experimental results of gradual porosity volumetric air receivers with wire meshes,” *Renew. Energy*, vol. 122, pp. 339–353, 2018.

[22] J. Moon *et al.*, “Black oxide nanoparticles as durable solar absorbing material for high-temperature concentrating solar power system,” *Sol. Energy Mater. Sol. Cells*, vol. 134, pp. 417–424, 2015.

[23] D. E. Karas, J. Byun, J. Moon, and C. Jose, “Copper-oxide spinel absorber coatings for high-temperature concentrated solar power systems,” *Sol. Energy Mater. Sol. Cells*, vol. 182, pp. 321–330, 2018.

[24] S. Mey-Cloutier, C. Caliot, A. Kribus, Y. Gray, and G. Flamant, “Experimental study of ceramic foams used as high temperature volumetric solar absorber,” *Sol. Energy*, vol. 136, pp. 226–235, 2016.

[25] C. K. Ho and J. E. Pacheco, “Levelized Cost of Coating (LCOC) for selective absorber materials,” *Sol. Energy*, vol. 108, pp. 315–321, 2014.

[26] T. K. Kim *et al.*, “Copper-alloyed spinel black oxides and tandem-structured solar absorbing layers for high-temperature concentrating solar power systems,” *Sol. Energy*, vol. 132, pp. 257–266, 2016.

[27] Y. S. Touloukian, R. W. Powell, C. Y. Ho, and P. G. Klemens, “Thermophysical properties of matter-the tprc data series. volume 1. thermal conductivity-metallic elements and alloys,” Thermophysical and electronic properties Information Analysis Center, 1970.

[28] J. Colas, L. Charpentier, and M. Balat-Pichelin, “Oxidation in Air at 1400 K and Optical Properties of Inconel 625, FeCrAlloy and Kanthal Super ER,” *Oxid. Met.*, vol. 93, no. 3, pp. 355–370, 2020.